REPORT DOCUMENTATION PAGE

Form Approved OMB No. 0704-0188

1. AGENCY USE ONLY (*Leave Blank*)	2. REPORT DATE	3. REPORT TYPE AND DATES COVERED
	November 1999	

4. TITLE AND SUBTITLE

High Speed Quantum Device and Circuits: Modeling and Design

5. FUNDING NUMBERS

6. AUTHOR(S)

H.L. Grubin
R.C. Buggeln

7. PERFORMING ORGANIZATION NAME(S) AND ADDRESS(ES)

Scientific Research Associates, Inc.
30C Hebron Avenue, P.O. Box 1058
Glastonbury, CT 06033-6058

8. PERFORMING ORGANIZATION REPORT NUMBER

9. SPONSORING/MONITORING AGENCY NAME(S) AND ADDRESS(ES)

Office of Naval Research
Ballston Tower One
800 North Quincy Street
Arlington, VA 22217-5660

10. SPONSORING/MONITORING AGENCY REPORT NUMBER

11. SUPPLEMENTARY NOTES

12a. DISTRIBUTION/AVAILABILITY STATEMENT

Approved for public release; distribution unlimited.

12b. DISTRIBUTION CODE

13. ABSTRACT (*Maximum 200 words*)

This document summarizes work carried out under a U. S. Navy SBIR study, Topic N99-02. The goal of the study was to develop a robust, portable, user-friendly, validated quantum device algorithm for designing tunneling devices, in particular resonant tunneling devices, for realistic present, near future and future applications. Successful algorithm development based on the space and time dependent Wigner equation was undertaken with the result that SRA has, in place, a transient algorithm for calculating the switching properties of resonant tunneling devices under a variety of conditions. The algorithm includes design information with respect to contacts, dissipation and the external circuit. The effects of noise were briefly studied, and recommendations were made for further work to permit the implementation of the algorithm for the design of a 100+GHz clock.

14. SUBJECT TERMS

Dissipation, Quantum Transport Barriers, Wells, Wagner Functions, GUI

15. NUMBER OF PAGES

34

16. PRICE CODE

17. SECURITY CLASSIFICATION OF REPORT	18. SECURITY CLASSIFICATION OF THIS PAGE	19. SECURITY CLASSIFICATION OF ABSTRACT	20. LIMITATION OF ABSTRACT
UNCLASSIFIED	UNCLASSIFIED	UNCLASSIFIED	UL

Scientific Research Associates, Inc.

Phase I SBIR Final Report for Navy Topic N99-02

High Speed Quantum Device and Circuits: Modeling and Design

PI: H. L. Grubin
Co PI: R. C. Buggeln

Submitted to the Office of Naval Research

November 1999

Phase I SBIR Final Report for Navy Topic N99-02

High Speed Quantum Device and Circuits: Modeling and Design

Abstract

This document summarizes work carried out under a U. S. Navy SBIR study, Topic N99-02. The goal of the study was to develop a robust, portable, user-friendly, validated quantum device algorithm for designing tunneling devices, in particular resonant tunneling devices, for realistic present, near future and future applications. Successful algorithm development based on the space and time dependent Wigner equation was undertaken with the result that SRA has, in place, a transient algorithm for calculating the switching properties of resonant tunneling devices under a variety of conditions. The algorithm includes design information with respect to contacts, dissipation and the external circuit. The effects of noise were briefly studied, and recommendations were made for further work to permit the implementation of the algorithm for the design of a 100+GHz clock.

Phase I SBIR Final Report for Navy Topic N99-02

High Speed Quantum Device and Circuits: Modeling and Design

Table of Contents

Phase I SBIR Final Report for Navy Topic N99-02

1. Introduction

This report summarizes work carried out under a U. S. Navy, Office of Naval Research, SBIR study. Also included is a summary of the option tasks and recommendations.

2. Background

There are high-speed signal-processing applications that would benefit from an **electronic oscillator** producing picosecond pulses with excellent timing stability, which can be locked to an external clock. Presently, excellent timing stability can be achieved with **opto-electronic conversion** generated pulses when a mode-locked laser is used as the source. But very recent experiments have demonstrated that resonant tunneling relaxation oscillators (RTRO) could emit sharp current pulse sequences that are mode locked to the fundamental mode of a cavity formed by a short circuit transmission line. The RTRO exhibited extremely low phase noise; in particular at **1.142 GHz** the phase noise at a 1kHz offset from the carrier was –88dBc/Hz[1]. By way of reference a hybrid superconductor/GaAs MESFET operating at 77K displayed a phase noise at a 10kHz offset equal to –87dBc/Hz [2]. SPICE-type simulations of the RTRO suggest that the device could oscillate at a repetition rate in excess of 150 GHz. **In other words there is the realistic prospect of developing an external clock operating in excess of 150 GHz.**

While the phase noise measurement for the RTRO was at frequencies significantly below that of the MESFET/superconducting combination [2], the basic element of the RTRO is the resonant tunneling diode (RTD). The RTD is part of a family of tunneling devices currently being developed for both commercial and military applications; in particular a resonant inter-band tunneling diode is currently being pursued for use in a 100 GHz clock [3], as displayed in figure 1. Thus, it is realistic to plan for very high speed digital clocks using RTDs.

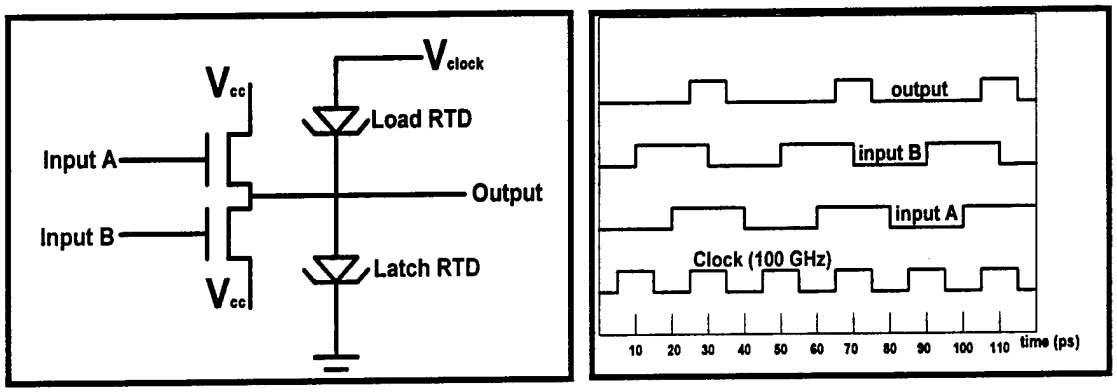

Figure 1. High-speed 100 GHz clock based on resonant interband tunneling devices [3].

In addition to the above there was a recent discussion [4] of a new RTD-FET family of clocked logic gate devices based upon RTDs. Simulations using SPICE show that the RTD circuits can achieve high performance in terms of speed and power in many signal-processing applications. **Compared** to III-V FETs alone the RTDs are predicted to

show factors of two improvements in speed at the same power levels. **Compared** to circuits using fully depleted CMOS the RTDs are predicted to operate five times faster when using the same CMOS design rules. (The RTD analysis was based upon assumed peak operating currents, peak-to-valley current ratios and other key device parameters.)

Thus we are faced with an emerging class of devices with a potential for extremely high speed with low noise and jitter. We anticipate that these devices will provide sampling rates in excess of 100G/sec with effective bits in excess of the '4' expected now. This is significant as these new devices may realistically enable workers to:

1.Overcome system/circuit receiver noise
2.Digitize microwave/MM transmit signals
3.Provide versatile synthesis and beam steering
4.Obtain faster signal processing

In short, the impact of the above is improved system performance and reduced life cycle cost.

The above discussion outlines the broad appeal of resonant tunneling devices for both military and commercial applications. But these RTDs are complex in their physics and in their system implementation. And, as is the case of devices that are part of the mainstream and are responsible for the personal computer industry, the design of RTDs rest heavily on numerical simulation and validation. Under the Phase I SBIR, SRA has been numerically simulating the large signal time dependent properties of these tunneling devices (figure 2 displays a schematic of the RTD).

The solutions arise from coupling of the time dependent quantum transport Wigner equation of motion and Poisson's equation, and incorporate dissipation. The transient behavior is large signal, incorporates displacement current and contact contributions and the results display the switching characteristics commonly associated with double barrier resonant tunneling diodes. These results will be displayed later in this report proposal. **The SRA simulations are potentially capable of providing all of the data necessary for incorporation into the SPICE simulations, and for providing RTD device design and material configurations.**

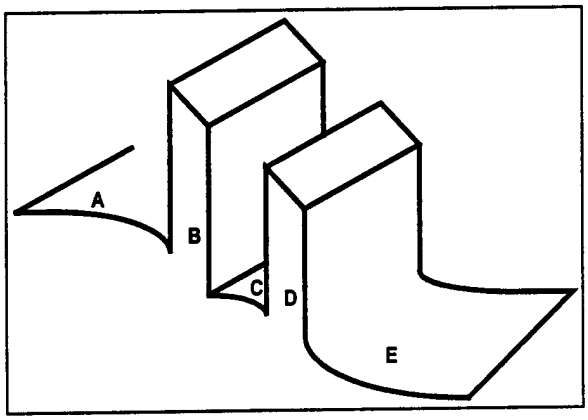

Figure 2. Schematic of the RTD Conduction Band Structure.

3. The Objectives of the Phase I SBIR Study

Most of the objectives of the Phase I study have been met. The remaining will be completed during the option phase. These objectives (*italicized*) included:

1. ***Further development and subsequent implementation of an existing time-dependent quantum transport algorithm.*** The algorithm of choice at SRA is the time dependent Wigner equation of motion. Transient implementation of this code has been successful and will be discussed more fully in **Section 4**. Incorporation of hole transport is currently under way. Variable effective mass and band structure generalizations will be performed during the option period.
2. ***Determine the transient response of devices with different material components to signals of different amplitude, rise times, dc bias levels.*** Picosecond and smaller switching times were computed under space charge conditions and are discussed in detail in **Section 4.** The transient response under different rise times and dc bias levels has been and will continue to be performed. The response of structures with different material properties, doping, barrier heights and widths has been undertaken.
3. ***Find a means of addressing the role of dissipation in RTD models and its effect on device performance.*** Dissipation has played a key role in the initial algorithm develop and will continue to be undertaken throughout the course of the study. The closer we achieve a realistic description of dissipation, the more accurate will be the computation of the device current-voltage relation and the transients. We have begun to examine the response of the device to different scattering events.
4. ***Develop a user-friendly interface, in which the user need only know what elements are necessary to construct a device. No knowledge of either the equations or the algorithm for solving the equations should be necessary. The algorithm should include output that can be transported to commercially available circuit design programs. A user-friendly interface will be accessed, and will provide a key entry into commercialization of the software.*** This work is continuing! However, using its own financial resources SRA purchased a Fortran compiler from the Portland Group. This compiler can be used on both UNIX, Linux or NT based systems and has Fortran 77 as well as Fortran 90 capabilities. This compiler means that anyone with the Microsoft NT4 operating system can use the SRA Wigner code. We are currently writing a short description of the procedures necessary to get this code working on NT4 platforms.
5. ***Verify the theoretical predictions of the software through comparison with experiment.*** This part of the study is necessary to gain broad acceptance by the community. The Principle Investigator will achieve experimental verification through contacts with colleagues in the field, and via a literature search. This is an option task.
6. ***Choose a demonstration device/circuit design for achieving 100 GHz logic, as a demonstration of the efficacy of the program.*** This is an option task.

4. The Phase I Results

4.1 Introduction

The initial effort in the Phase I study was the development of the large signal time dependent Wigner simulation algorithm. This effort is the core of the study. But the degree of significance of these simulations lies in the ability to predict device behavior in circuits of interest. Thus part of the Phase I study included circuit issues and how the device properties would influence them. We begin the discussion of the Wigner simulation with the circuit considerations.

4.2 The RTD in a Circuit/System-The Basic Issues

What are the basic issue(s)? We are dealing with a very fast device, a device whose leading and trailing transient edge is of the order of 1ps or shorter. The device can be incorporated into a circuit and designed to function as the primary architectural element of multiple value logic. The device can also operate as a self-excited relaxation oscillator with frequencies in the THz range, as a forced oscillator, and as an element in a high-speed clock.

It is the self-excited relaxation oscillator that was of most interest to us because the structure of the electrical output can contain significant harmonic contributions, suggesting:

1. The electrical output can be tailored to a near square-like waveform, and
2. Operation involving higher harmonics is possible.

First let us see how this harmonic contribution comes into play and how we can utilize the dynamic operation of the device to achieve this type of operation.

Approximately 40 years ago Leo Esaki [5] described the electrical operation of a tunnel diode. Like the double barrier resonant tunnel diode, also first discussed by Esaki (and co-workers), the tunnel diode displays a current voltage characteristic with a region of negative differential resistance. Because the tunnel diode is a low frequency device it has been possible to discuss its behavior in an external circuit in terms of lumped element circuit parameters. Within the framework of this picture the tunnel diode is visualized as a nonlinear resistor in parallel with a capacitor. If we place this device in a circuit containing lumped reactive circuit elements and switch on an external dc source with a sufficiently high voltage, there will be transient voltage swings though three regions: (a) a low voltage resistive region, (b) an intermediate voltage, and (c) a high voltage resistive region. This is represented schematically in figure 3a, where the tunnel diode is represented as a nonlinear 'N' [6] shaped negative differential resistor in parallel with a capacitor.

For this configuration, with the voltage swing **sampling either the low voltage or the high voltage portion** of the nonlinear resistor, any incipient oscillation is damped. But if the voltage also samples the region of negative differential conductivity then the possibility of sustained self-excited oscillations emerges.

Self-excited oscillations have often been generically linked to the van der Pol oscillator as well as Gunn effect oscillators, see PI monograph [7]. Self-excited Gunn oscillators were called LSA (large signal amplitude) oscillators and the PI undertook a detailed study of them in the late 60's and early 70's. The principle relevance of Gunn self-excited oscillator studies for the RTD is the observation that space charge effects often determined the range of frequency accessible to the Gunn diode, and by extension may determine the frequency range of the RTD oscillator. **Thus one key recommendation is**

to determine in what manner the space charge within the RTD affects the frequency range of operation of the circuit.

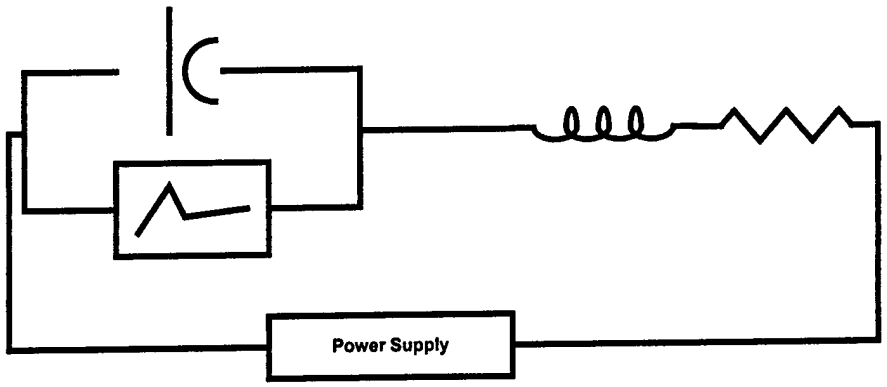

Figure 3a. Lumped element circuit with an active nonlinear element. The circuit is capable of sustaining self-excited oscillations.

But the RTD has also been operated as a self-excited relaxation oscillator [1] in the configuration shown in figure 3b, and at frequencies slightly in excess of 1 GHz. This result suggests that self-excited oscillations can provide a steady stream of voltage pulses and thereby the basis for a high GHz clock. It is this result that provides the compelling reason to simulate this type of RTD application. In fact, for the frequency range of interest, simulations involving transmission lines are much more realistic providing the device it not represented as a lumped equivalent element, but as a solution to the Wigner equation.

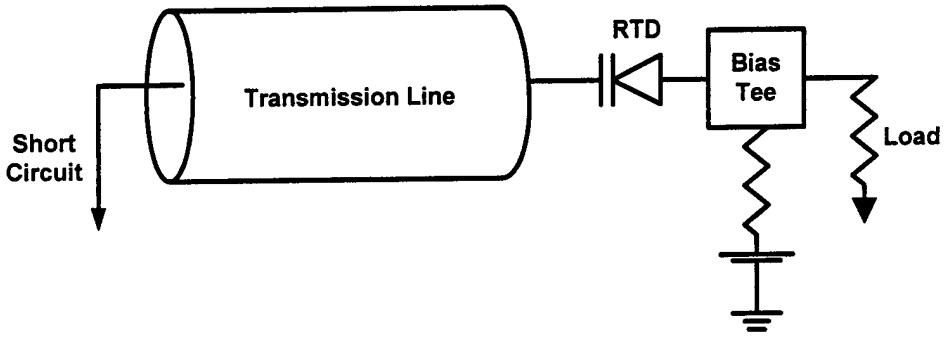

Figure 3b. Schematic of the experimental configuration in which an RTD exhibited self-excited oscillations and frequencies in excess of 1 GHz (from [1]).

While the general approach discussed above forms an important part of the proposed Phase II proposal, considerable insight into device operation was obtained during the Phase I study by performing **simulations in a lumped element circuit** with the device represented as a nonlinear resistor in parallel with a capacitor. In performing these simulations we were able to uncover information about the noise characteristics of the RTD operating as a relaxation oscillator and the ability of the circuit to, in some cases suppress the noise. This will be discussed next.

4.3 Lumped Element RTD Circuit Simulations-Relaxation Oscillations

Ignoring the external resistor the two relevant circuit equations corresponding to figure 3a are:

$$(1)\qquad \begin{aligned} V_{Bias} &= V_D + L\frac{dI}{dt} \\ I &= C\frac{dV_D}{dt} + I_D(V_D) \end{aligned}$$

In the above V_D represents the voltage across the nonlinear resistor and I is the current through the NDR element and the capacitor. Experience with the above equations [7] teaches that for a particular nonlinear element the character of the oscillation is determined by only ***two*** parameters (part device, part circuit parameters). And it is these parameters that control whether or not the oscillation is a relaxation oscillation. These parameters are extracted in the simplest case of figure 3a by introducing the following normalizing parameters:

(2) **Peak Current**: I_P; **Voltage at** I_P: V_P; **Normalized Time**: T

With these quantities, equation (1) is re-expressed in terms of normalized time dependent voltage and current:

$$(3)\qquad \begin{aligned} \frac{dv_D}{d\tau} &= \frac{I_P T}{CV_P}\left\{i - i_D(V_D)\right\} \\ \frac{di}{d\tau} &= \frac{V_P T}{LI_P}\left\{v_{Bias} - v_D\right\} \end{aligned}$$

Here:

$$(4)\qquad \begin{aligned} v_D &= V_D / V_P \\ i &= I / I_P \\ \tau &= t / T \end{aligned}$$

If we express the normalized time in terms of the standard reactive circuit elements, $T = 2\pi\sqrt{LC}$, and introduce a device resistance as $R_D = V_P / I_P$, and a circuit impedance $Z_0 = \sqrt{L/C}$, then the circuit equations (1) become

$$(5)\qquad \begin{aligned} \frac{dv_D}{d\tau} &= \frac{2\pi Z_0}{R_D}\left\{i - i_D(V_D)\right\} \\ \frac{di}{d\tau} &= \frac{2\pi R_D}{Z_0}\left\{v_{Bias} - v_D\right\} \end{aligned}$$

Where are we going with this? Let us take values for the reactive components such that their product is constant and yields a nominal oscillation period of $10\,ps$. Within this constraint we chose two different values for the ratios Z_0 / R_D. The results are dramatically different. In figure 4a this ratio is $Z_0 / R_D = 50/2\pi$, whereas in figure 4b this ratio is $Z_0 / R_D = 10/2\pi$. What are these differences and are they important? First, both cases yield self-excited oscillations, but with different oscillation periods. For $Z_0 / R_D = 50/2\pi$, the oscillation period is approximately $18\,ps$, for a frequency near

$50GHz$. For $Z_0/R_D = 10/2\pi$ the period of oscillation is approximately $14\,ps$, for a frequency near $70GHz$. But more significant is the amplitude of the voltage and current oscillation. The ratio of voltage to current is significantly larger in the former case, and the structure of the voltage oscillation contains significantly more harmonic contributions in the former case. **Further the large voltage oscillation appears to be closest in form to a square wave oscillation.**

What does this signify? In earlier work on Gunn effect oscillations [7] a characteristic property of these devices was the presence of highly a nonuniform space charge distribution that could control the property of the oscillation. Oscillations with large voltage swings were the most effective in suppressing incipient space charge effects and were often responsible for circuit control of the oscillation. The situation with the RTDs, particularly with respect to hysterisis and perhaps noise, will remain unknown until the device, rather then being represented by an equivalent circuit model is represented as a solution to the Wigner equation of motion. **But the question that needs to be answered is whether the external circuit rather than the device is the primary controller of the self-excited oscillation.**

4.4 RTDs and Noise

The next issue is the role of noise on the oscillation. The observation of [1] was that the RTD when operated as a relaxation oscillator exhibited extremely low noise properties. How are we to assess the way noise affects the operation of this device? There is noise in all circuit elements, including the external impedances. But of interest is the noise associated with the RTD.

To address this issue we performed some very preliminary calculations. Fluctuations within the RTD will affect the space charge distribution within the RTD and will consequently affect the current voltage relation of the RTD. Indeed, if we were to exaggerate this effect we would expect a current voltage RTD relation of the type shown in figure 5, where we see considerable noise. This noisy current versus voltage relation should be regarded as a snapshot of the RTD IV relation, because it will evolve in time. What could be the origin of this noise? Certainly we expect scattering events to contribute. In addition we expect fluctuations in the background charge density, and the presence of other structures in the immediate environment to contribute. In any case noise is expected to affect the current voltage relation of the RTD. **Is a noisy IV curve detrimental to device performance?** Intuitively one would expect this to be the case.

There are several levels on which to examine the effects of noise on device performance. The one we chose initially was to determine if a noisy device would alter the phase and or amplitude of the oscillation. Thus for a given nominal set of device and circuit parameters we performed pairs of calculations. These pairs consisted of a **control** calculation in which the device IV curve did not contain any noisy components, and a **model** calculation in which the IV curve was similar to that of figure 5. The word similar is used because each time we performed a calculation the noisy IV curve was changed.

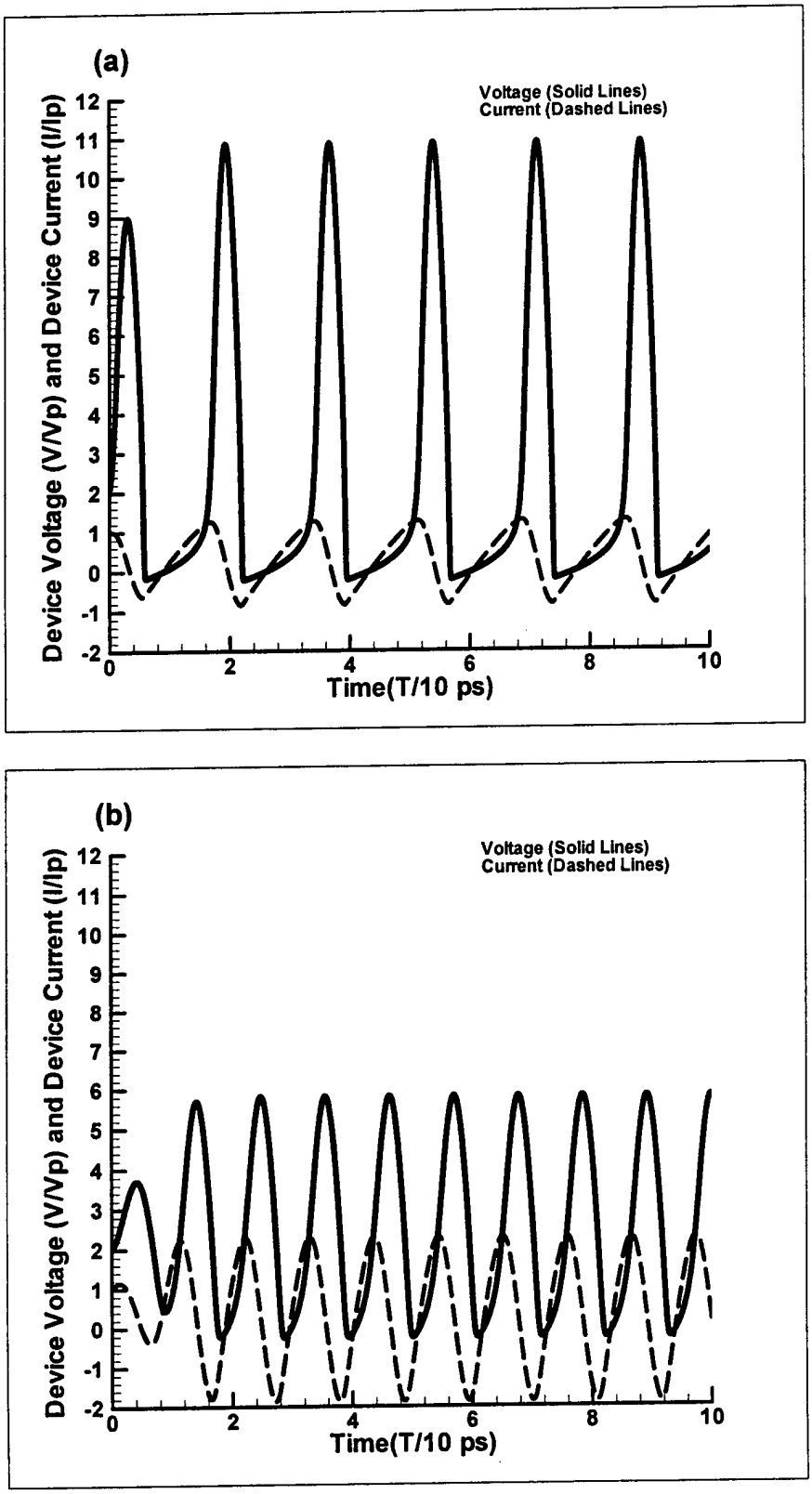

Figure 4. Large signal relaxation voltage and current versus time for a circuit with the same resonant frequency. (a) $Z_0 / R_D = 50/2\pi$ *, (b)* $Z_0 / R_D = 10/2\pi$

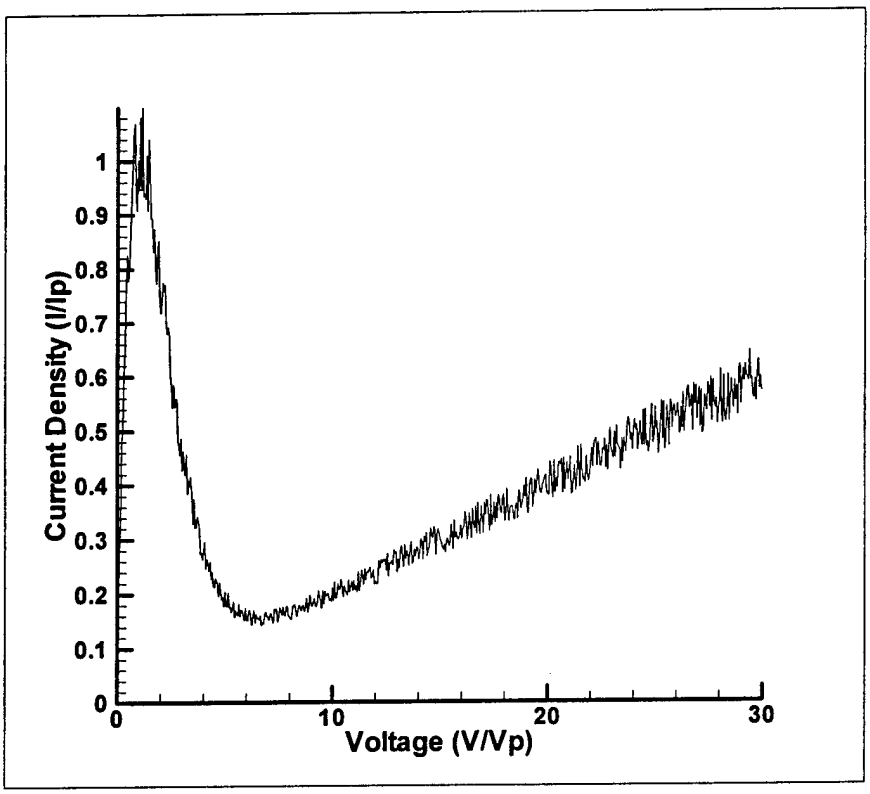

Figure 5. Random fluctuations superimposed on an assumed current density versus voltage curve for an RTD.

For the parameters of figure 4a, where $Z_0 / R_D = 50/2\pi$, the results are shown in figure 6a. The solid curve in figure 6a is a repeat of the voltage curve in figure 4a. The dashed curve is obtained with the noise contribution. Note that the dashed curve is shifted away from the solid curve, and that the phase shift appears to be time dependent. Also there is a modification in the amplitude of the oscillation. Carrying out the calculation for longer time periods does not alter the nature of the drift of the oscillation. Since the IV characteristic changes with time the steady drift in the phase, as seen in figure 6a would not occur, rather there would be random variations in the phase and amplitude. **But we can conclude that noise variations in the current voltage relation of the RTD IV characteristic result in both amplitude and phase noise for this set of circuit parameters.** This result is expected.

The results for the case $Z_0 / R_D = 10/2\pi$, where the voltage amplitude is reduced are shown in figure 6b. There is still the presence of phase noise although it is somewhat reduced. The conclusion of figure 6 is that **the circuit can modify the deleterious effects of the noise in the RTD.**

But there is a large phase space available to circuit designers and these results suggest that a clever designer could reduce the noise to manageable levels. This is a result that we were able to demonstrate! We performed simple calculations in which the only change was the dc bias across the structure. For the circuit in which $Z_0 / R_D = 50/2\pi$, we continued to observe phase noise for those situations in which the

dc bias was raised to significantly higher levels while still maintaining circuit controlled self-excited oscillations. ***However, for the circuit with*** $Z_0 / R_D = 10/2\pi$ ***, it appeared, visually, that the noise was absent.*** This rather remarkable results provides a strong reason to examine, in detail, the role of the circuit in either enhancing or suppressing noise in circuits with RTDs.

4.5 RTDs and Transmission Lines

There is at least one aspect of the problem that needs to be generalized, and this is the self-consistent device circuit simulations. We are presently developing the capability to perform transient accurate Wigner simulations with the device connected to an external circuit. Results will be forthcoming during the option period. This places SRA in the position of performing simulations that are significantly more involved than the simpler SPICE calculations where the device is represented by an equivalent circuit element. But even with the more realistic representation of the device, we do not have a realistic representation of the circuit. The frequencies of interest in the study are too high for an adequate lumped element representation of the circuit. **Since a key goal of the program is to provide software that is useful in the design of very high speed devices, then we need to go to the next step and provide studies within the framework of distributed elements or transmission lines.**

As a head start on this problem we have begun to look at simple autonomous transmission lines that include a nonlinear resistor, (see figure 7 for one section of the transmission line) the simplest equations are generalized as follows:

$$\frac{\partial V(x,t)}{\partial x} = -L\frac{\partial I(x,t)}{\partial t}$$

$$\frac{dI(x,t)}{dx} = -C\frac{\partial V(x,t)}{\partial t} - J(V) \qquad (6)$$

The term $J(V)$ represents the nonlinear negative differential conductivity. Please note that there is a developed body of literature on this problem [8]. We have begun to solve these equations and expect to have preliminary results for the case where the RTD is represented by equivalent circuit parameters.

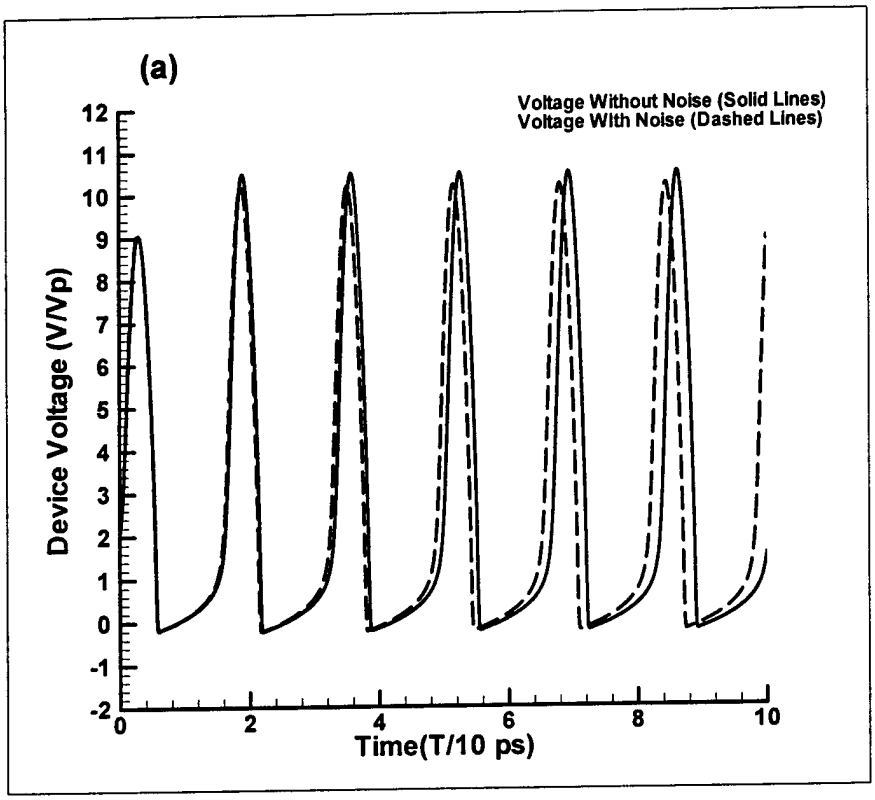

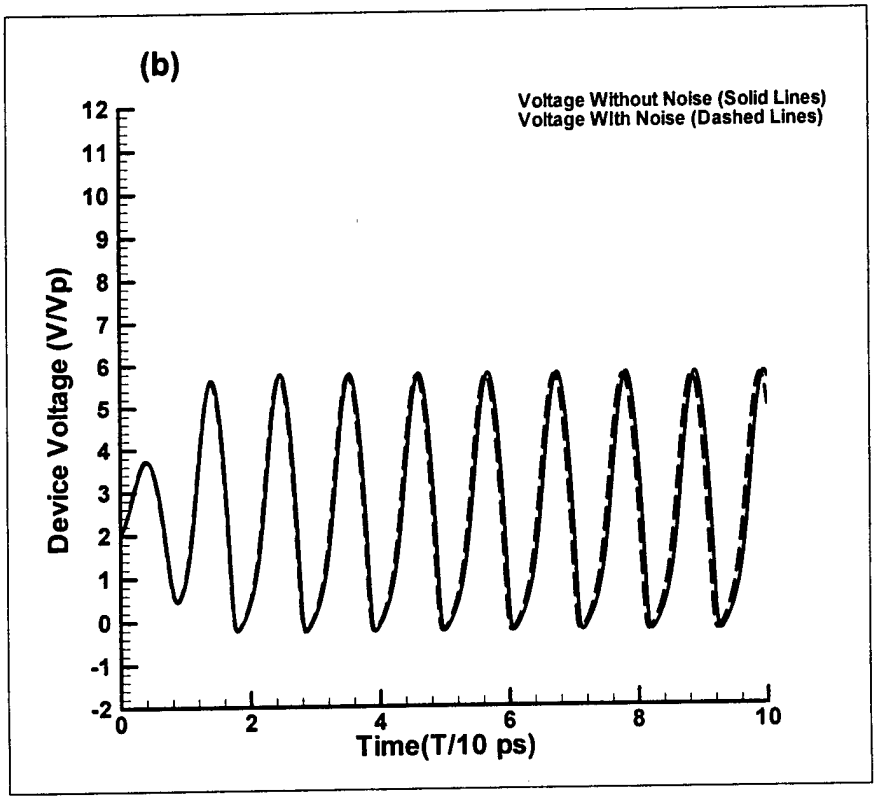

Figure 6. Voltage versus time for the same circuit parameters as figure 3. These figures also include a calculation in which the current-voltage relation is noisy as represented by figure 4.(a) $Z_0 / R_D = 50/2\pi$ *, (b)* $Z_0 / R_D = 10/2\pi$

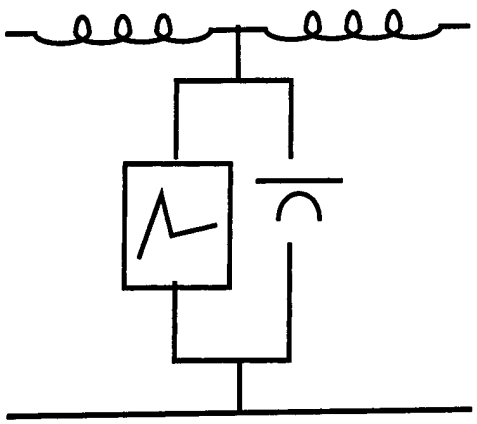

Figure 7. Sketch of one section of an autonomous transmission line containing a nonlinear negative differential resistor.

4.6 The Quantum Transport Equation

The present situation is that the RTD is a viable device for high-speed low noise operation. What is needed is a design tool that is cost effective in terms of computational time, contains the relevant physics, is capable of being modified by the user, and contains the relevant circuit models.

The basis for this was discussed in the Phase I proposal, and the initial implementation was within the framework of the time dependent Wigner equation of motion, **where transients, contacts, and dissipation were dealt with!** What is this equation? What are (is) the quantum mechanical contributions? What is unique about the approach at SRA?

The approach taken during the Phase I study was to solve the Wigner equation of motion [9]. The advantage of the Wigner function is that momentum dependent band structure can readily be incorporated, particularly with respect to the constraints of transverse momentum. Additionally, as the results demonstrate, transients can be studied with relative ease. The Wigner equation is also a vehicle with which device-device interaction can be handled.

The Wigner equation, incorporating dissipation is:

$$\frac{\partial f_w(\mathbf{k},\mathbf{r},t)}{\partial t}+\left(\frac{\partial f_w(\mathbf{k},\mathbf{r},t)}{\partial t}\right)_{DISSIPATION}+\frac{\hbar\mathbf{k}}{m}\cdot\frac{\partial f_w(\mathbf{k},\mathbf{r},t)}{\partial \mathbf{r}}$$

$$+\frac{i}{\pi^3\hbar}\int d^3r'\left[V(\mathbf{r}+\mathbf{r}',t)-V(\mathbf{r}-\mathbf{r}',t)\right]$$

$$\times\int d^3k' f_w(\mathbf{k}',\mathbf{r},t)\,exp2i(\mathbf{k}'-\mathbf{k})\cdot\mathbf{r}'=0 \qquad (7)$$

In the above $f_W(\mathbf{k},\mathbf{r},t)$is the Wigner distribution function. $f_W(\mathbf{k},\mathbf{r},t)$ does not represent a probability distribution as it can assume negative values. The term $V(\mathbf{r},t)$ appearing in equation (7) is the potential that appears in the dissipationless Schrodinger equation, and includes the barriers, the self-consistent potential from Poisson's equation, any exchange interaction, etc. The charge density and current density required for determining the response of the quantum structure to the imposed excitation is obtained from the Wigner function through the standard expressions (for electrons):

$$(8)\qquad n(\mathbf{r},t)=-\frac{e}{4\pi^3}\int d^3k f_W(\mathbf{k},\mathbf{r},t);\quad \mathbf{j}(\mathbf{r},t)=-\frac{e}{4\pi^3}\int d^3k\frac{\hbar\mathbf{k}}{m}f_W(\mathbf{k},\mathbf{r},t)$$

In equation (7) dissipation is represented by the term with the subscript "*DISSIPATION*". And all quantum transport is contained within the integral contribution of equation (7). The barriers and the solution to Poisson's equation are contained in the term $V(\mathbf{r})$, whose argument is skewed in equation (7). This integral contribution reduces to the standard derivative commonly found in the Boltzmann equation, when the potential energy contains contributions only from Poisson's equation. Under the Phase I study to date we concentrated only on single-band-single-species (electron) transport. Within this framework the constraint imposed on the scattering was that the electron trajectory in real space is continuous even though electrons are scattered from one quantum state to another [10], [11], i.e.:

$$(9)\qquad 0=\int d\mathbf{k}\left(\frac{\partial f_w(\mathbf{k},\mathbf{r})}{\partial t}\right)_{DISSIPATION}$$

$$(10)\qquad \left(\frac{\partial f_w(\mathbf{k},\mathbf{r})}{\partial t}\right)_{DISSIPATION}=\frac{f_w(\mathbf{k},\mathbf{r})-f_{w0}(\mathbf{k},\mathbf{r})\{\rho(\mathbf{r})/\rho_0(\mathbf{r})\}}{\tau(\mathbf{r})}$$

In subsequent calculations, the above constraint has been removed. Presently, in addition to calculations subject to equation (9) we are performing standard relaxation time calculations as well as a combination of the standard and non-standard relaxation time (equation (9)) studies. The standard relaxation time studies yield a source term in the Wigner equation

In all of the studies discussed below we include Poisson's equation:

$$(11)\qquad \nabla^2 V_{POISSON}(\mathbf{r},t)=-\frac{e^2}{\varepsilon}(\rho(\mathbf{r},t)-\rho_0(\mathbf{r}))$$

The physical model we are using for the calculation is represented in figure 8, with the device consisting of three regions. Equation (7) is solved in all three regions, but regions '1' and '3' are modeled as resistors and are dissipative. Region '2' contains barrier/well combinations and also includes dissipation. The transition from the quantum to the classical region is determined by the user, as are the dimensions of the 'classical' regions. There are numerous advantages to this approach, which requires validation, the first is that a string of RTD connected in series can be treated using the same algorithm (sic, the same matrix inverter), and that physical boundary conditions (e.g. contacts) can be realistically treated. **Note: the user is under no obligation to include a classical region.**

While the Phase II study will permit a spatially dependent effective mass, the results discussed below are for a constant effective mass. During the Phase I option period we will concentrate on generalizing the Wigner equation of motion. Please recall that for the density matrix the spatially dependent effective mass is introduced through the terms (for one spatial dimension):

$$(12)\qquad -\frac{\hbar^2}{2}\left[\frac{\partial}{\partial x}\left(\frac{1}{m(x)}\frac{\partial}{\partial x}\right)-\frac{\partial}{\partial x'}\left(\frac{1}{m(x')}\frac{\partial}{\partial x}\right)\right]\rho(x,x')$$

The modified Wigner equation is then obtained from the Wyle transformation.

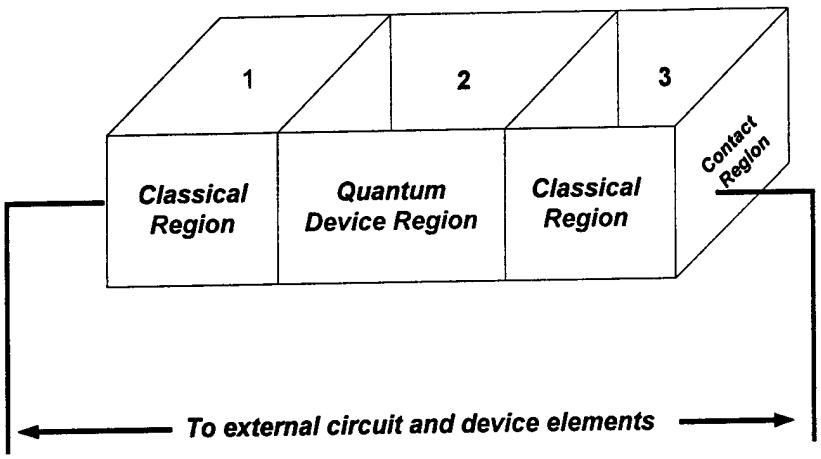

Figure 8. Physical model used for Wigner simulations.

We note that semiclassical representations of a position dependent effective mass would replace the term $\hbar\mathbf{k}/m\cdot\partial f_w(\mathbf{k},\mathbf{r},t)/\partial\mathbf{r}$ by $\hbar\mathbf{k}/m(\mathbf{r})\cdot\partial f_w(\mathbf{k},\mathbf{r},t)/\partial\mathbf{r}$. Quantum mechanical contributions are more tedious to deal with. For example, in a recent study [12], the $\hbar\mathbf{k}/m\cdot\partial f_w(\mathbf{k},\mathbf{r},t)/\partial\mathbf{r}$ term was replaced by

$$(13)\qquad \hbar\int_{-\infty}^{+\infty}\frac{dk'}{4\pi}\int_{0}^{+\infty}d\xi\cos[(k-k')\xi]\left(\frac{2}{m(x+\xi/2)}+\frac{2}{m(x-\xi/2)}\right)\frac{\partial f_W(k',x)}{\partial x}$$

There are other changes as well, but the Wigner potential (the integral contribution to equation (7)) is unaltered by the spatial variation in the effective mass. One of the Phase I tasks is to incorporate the variation in the effective mass. This will be completed in the Option Phase of the Phase I study.

The above equations have been programmed and applied to steady state and transient accurate investigations. We have examined classical problems as well as quantum mechanical problems. Often the classical problem was executed to provide checks on the algorithm. These studies included simple Ohm's Law studies in which the background density was kept constant, while the relaxation time was either spatially dependent or constant. Classical calculations were also performed with the background density reduced in value within the center of the structure. **These calculations also enabled us to conclude that any self-consistent open boundary device simulations for structures smaller than 200nm (the quantum mechanical regions could, of course, be as small as required) are likely to be incorrect. This issue is briefly discussed in the next section.**

4.7 Boundary Conditions

A few comments are in order on the role of the boundary. For the simulations of this study there are several crucial features we need to concern ourselves with.

The ends of the device are taken as reservoirs in which the carriers are in local equilibrium with the background. For this to occur we need a sufficient number of scattering mechanisms. Most device simulations, including ours do not treat the details of scattering in the vicinity of the contacts. Since we are interested in reservoir conditions, a

natural boundary condition for the ends of the device is a displaced Fermi distribution. Whether or not a displaced Fermi distribution within the boundary region is realistic is dependent upon the ability of the carriers to relax to this distribution after they traverse regions of strong potential variation. We performed simple calculations with a derivative boundary condition on the Wigner function, $\partial f/\partial x = 0$ and a constant relaxation time of 10^{-13} sec. We determined that that for structures $200\,nm$ long the carriers do not relax to a distribution approaching that of a displaced Fermi function. These simple calculations were for a classical $N^+N^-N^+$ structure. Decreasing the relaxation time to 10^{-14} sec, either uniformly or non-uniformly, in the vicinity of the boundary produced a distribution that had the shape of the displaced Fermi distribution. This is an important result, because it strongly suggests that forcing the boundary to represent reservoirs may not be compatible with the design of the device, particularly when the device is as small as $200\,nm$. Most of our current simulations are being performed with these less restrictive derivative boundary conditions.

There is also a bonus with these boundary conditions. In the initial transient simulations we used displaced Fermi distribution boundary conditions. This required an algorithm for computing the time dependent behavior of the displaced momentum and its relation to the electric field on the boundary. In other words we needed a model relationship for time dependence of the momentum. We chose the simplest Newton's law expression that included a frictional contribution. The result, while reasonable from a physical point of view is nevertheless model dependent. In the present scheme where we use the $\partial f/\partial x = 0$ condition, we are not forced to introduce this momentum-field relationship. Instead, the displacement current, which arises solely from Maxwell's equations, is not model dependent. These changes have been incorporated into the code in the past week. As such, the time dependent results displayed in the report below do not include these latest revisions to the algorithm.

4.8 Steady State Barrier Simulations

Steady studies of single and double barrier structures, as well as triple barrier structures were studied, although most of the effort was directed toward double barrier structures. Typical device structures studied were 200 nm long with parameters appropriate to GaAs. The effective mass was constant. For the illustrations below we deal with two 250 meV barriers, 5nm wide, separated by 5nm. The background doping was set to $10^{24}/m^3$ everywhere except for a 40nm wide region in the center of the structure where the doping was $10^{21}/m^3$. The transition from the low to high doping values occurred over a distance of 5nm on either side of the barrier. The contact regions on either side of the structure were each 15nm long with a scattering time of 10^{-14} sec. The scattering time in the remainder of the device was 10^{-12} sec. There is a gradual transition from the smaller to the large scattering time. The quantum contributions to the integral in the Wigner equation occurred over the center 120nm of the structure. The remaining parts of the structure were treated classically. This structure exhibited negative differential conductivity.

Solutions to the Wigner equation of motion yield the quantum distribution function $f(k_x, k_y, k_z, x)$. Because we deal with parabolic bands under the Phase I study,

symmetry dictates that the quantum distribution function is only a function of k_x and x. The equilibrium distribution function for this calculation is shown in figure 9. The equilibrium boundary conditions are appropriate to Fermi statistics and as we move toward the center of the device there is a decrease in the value of the distribution function. This yields a decrease in the particle density. The small position dependent structure near the tail of the distribution is a measure of the quantum mechanical barriers. In the absence of any barrier, this structure is flat. (As mentioned above the boundary conditions used in the program evolved during the course of the study. For the calculation of figure 9, and the remaining Wigner simulations, we assumed displaced Fermi distributions on the inflow boundaries. Newer calculations have been performed where the displaced distribution is replaced by the condition $\partial f / \partial x = 0$, on the inflow boundaries. The solution evolves towards a symmetric equilibrium Fermi distribution on the boundary, corresponding to the initial guess of a Fermi distribution.

The Wigner distribution was also computed as a function of bias. This dependence is shown in figures 10 and 11. The bias was increased in multiples of $k_B T$ or approximately 26 meV at room temperature.

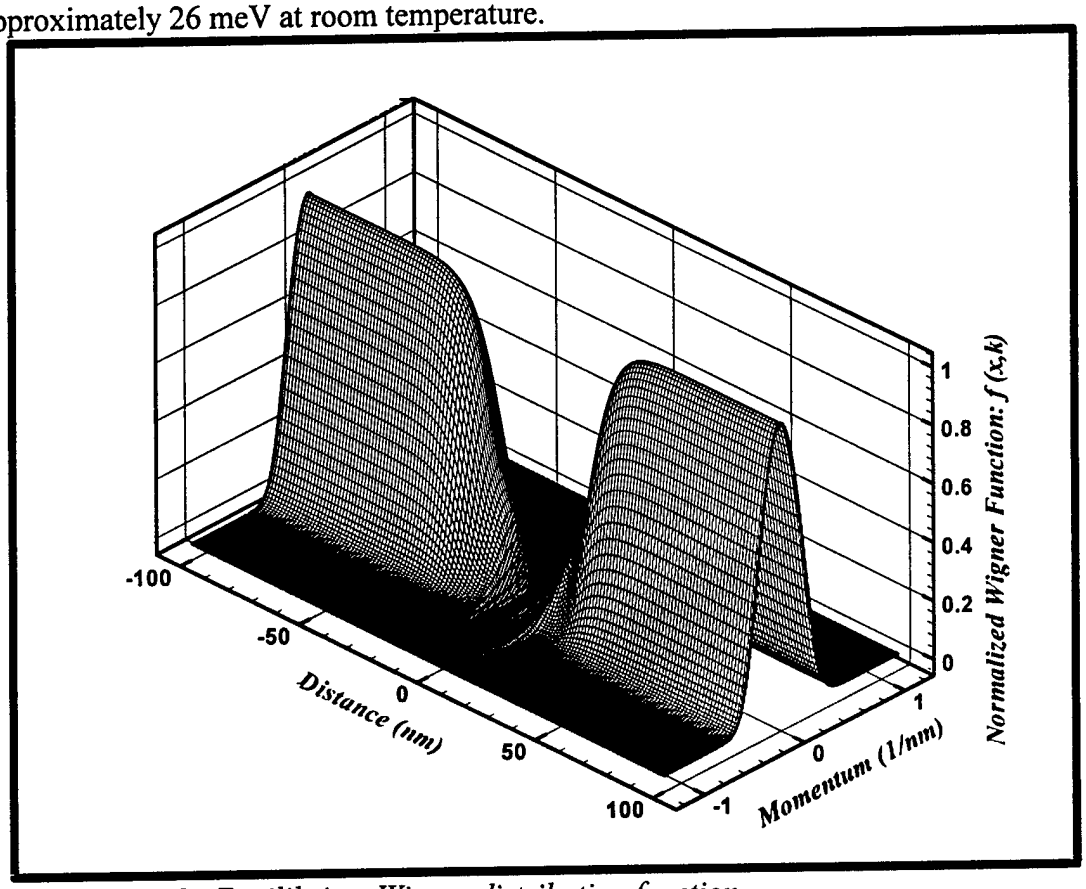

Figure 9. Equilibrium Wigner distribution function.

Figures 10 and 11 display the progressive increase in value of the quantum distribution in the center of the device. There is also some streaming on the upstream portion of the distribution that begins to settle into the calculation at approximately $-4k_B T$ in bias.

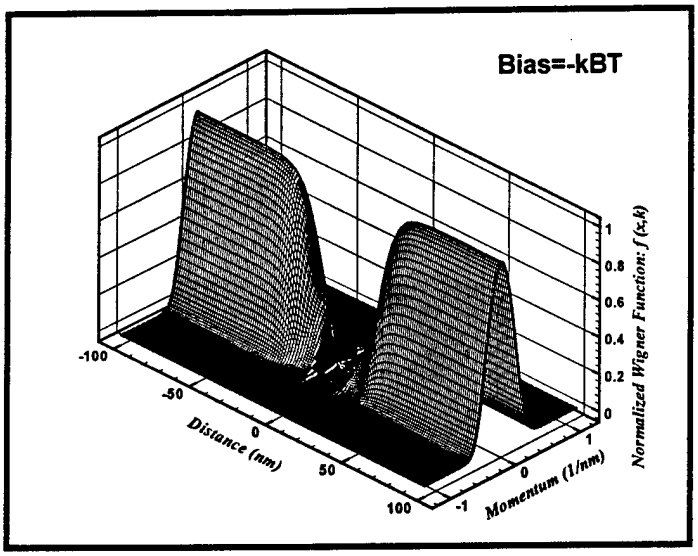
Bias=-kBT
Distance (nm)
Momentum (1/nm)
Normalized Wigner Function: f (x,k)

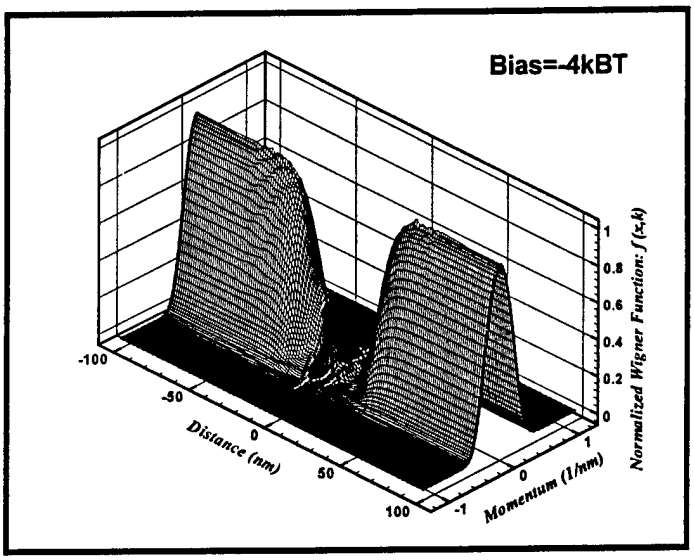
Bias=-4kBT
Distance (nm)
Momentum (1/nm)
Normalized Wigner Function: f (x,k)

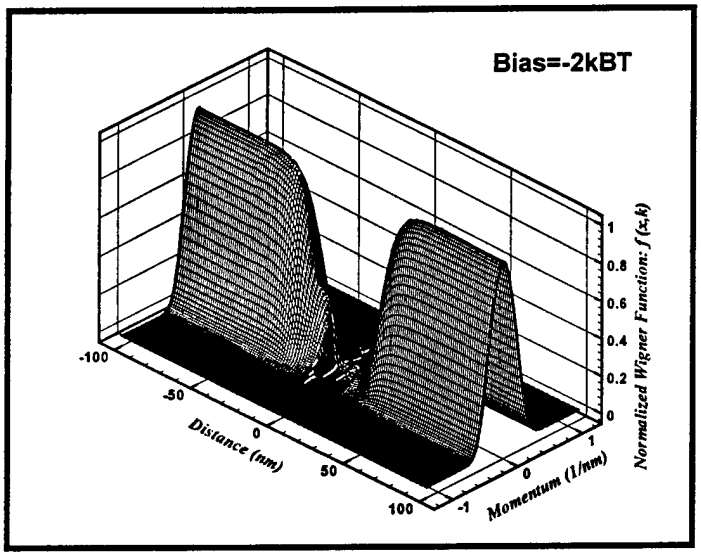
Bias=-2kBT
Distance (nm)
Momentum (1/nm)
Normalized Wigner Function: f (x,k)

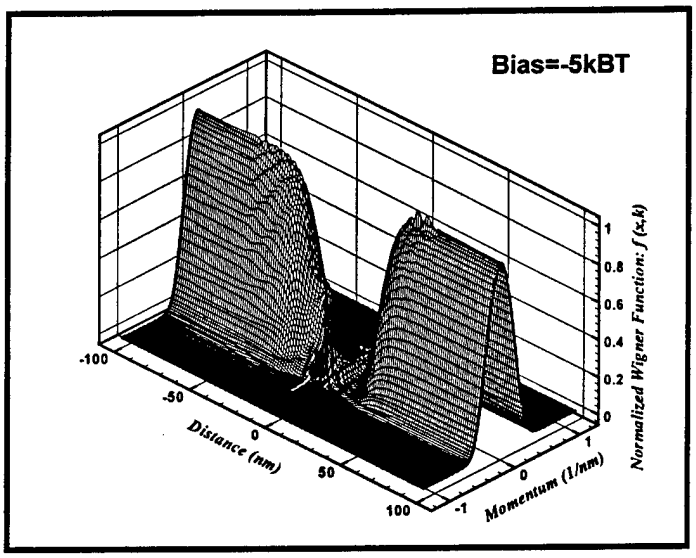
Bias=-5kBT
Distance (nm)
Momentum (1/nm)
Normalized Wigner Function: f (x,k)

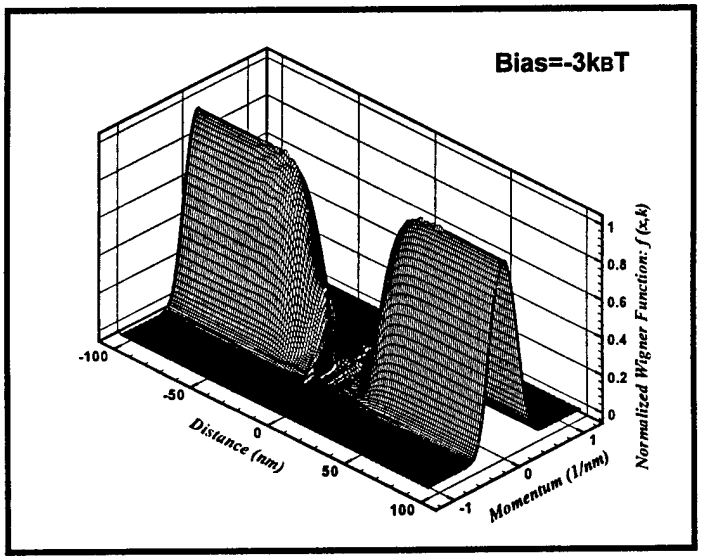
Bias=-3kBT
Distance (nm)
Momentum (1/nm)
Normalized Wigner Function: f (x,k)

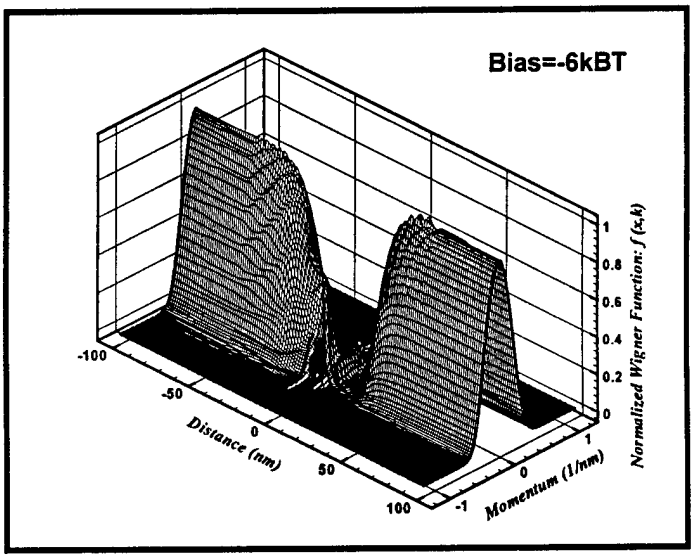
Bias=-6kBT
Distance (nm)
Momentum (1/nm)
Normalized Wigner Function: f (x,k)

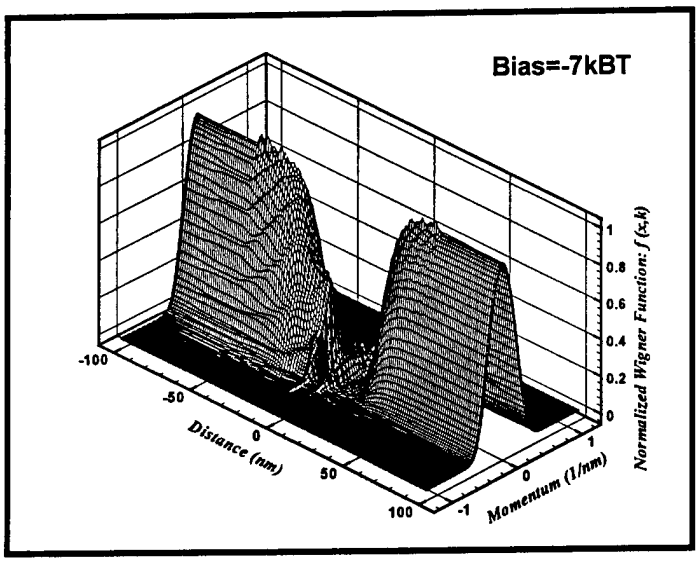
Bias=-7kBT
Distance (nm)
Momentum (1/nm)
Normalized Wigner Function: f (x,k)

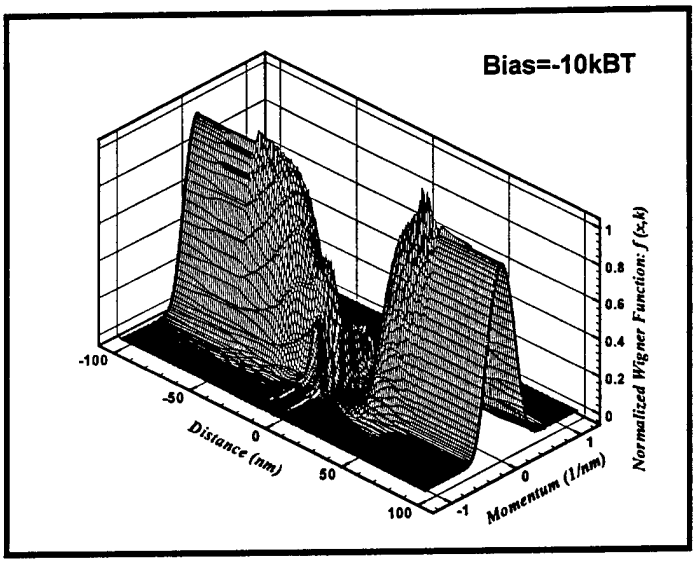
Bias=-10kBT
Distance (nm)
Momentum (1/nm)
Normalized Wigner Function: f (x,k)

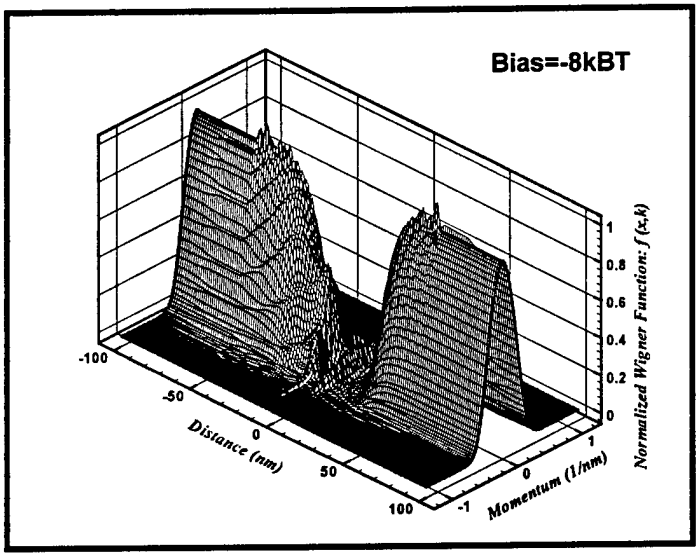
Bias=-8kBT
Distance (nm)
Momentum (1/nm)
Normalized Wigner Function: f (x,k)

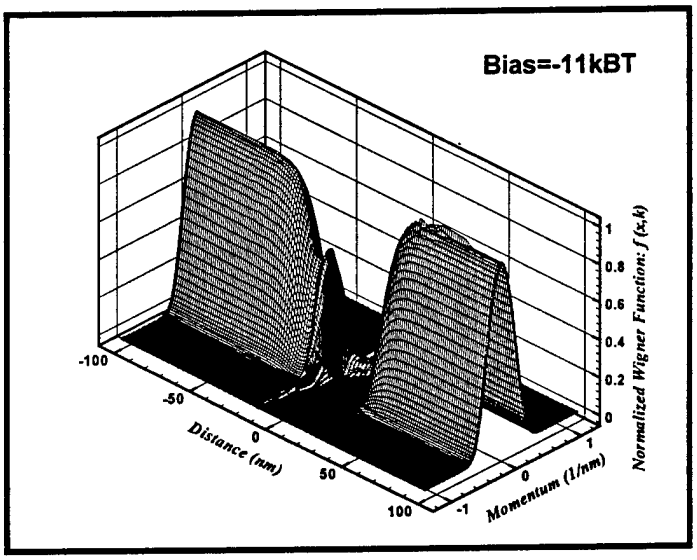
Bias=-11kBT
Distance (nm)
Momentum (1/nm)
Normalized Wigner Function: f (x,k)

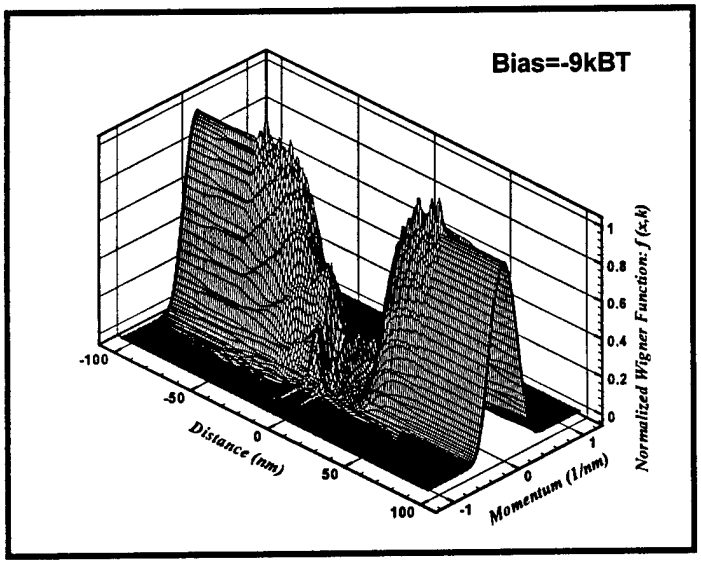
Bias=-9kBT
Distance (nm)
Momentum (1/nm)
Normalized Wigner Function: f (x,k)

There is also considerable noise in the calculation at higher bias levels that subsequently disappeared at a bias of $-11k_BT$. This noise is not physical. (Further study has demonstrated that larger numbers of grid points tend to eliminate the noise. Additionally, when the displaced Fermi distribution boundary condition by a derivative boundary condition there was a reduction in the numerical noise. We have begun to test the use of variable mesh spacing in the calculation to eliminate this noise.)

Of course, all of the information we get about particle density, current, etc is obtained from the Wigner equation (see equation (8)). The density distribution corresponding to the Wigner distribution is shown in figure 12. In figure 12 we display the density versus distance for values of bias ranging from $0 \geq V_{BIAS} \geq -11k_BT$. The peak current occurs when $-10k_BT$, which is approximately 260 meV.

Figures 12a and 12b contain the same data. The difference between the two is the curve that is being emphasized. In figure 12a the bold dashed line represents the density distribution **just prior to the drop in current.** In figure 12b, the bold solid line represents the density distribution **immediately after the drop in current**. The density distribution evolves with bias. As the collector is made more negative with respect to the emitter, there is a buildup of charge between the barriers as well as on the emitter side of the double barrier structure. This buildup continues for all values of bias until the peak value of current is reached. Charge conservation requires that a zone depleted of carriers form on the collector side of the structure. This is also apparent from the figure. Beyond the peak value of the current there is a precipitous change in the distribution of charge. The quantum well is depleted of charge, with a corresponding extreme buildup of charge on the emitter side of the double barrier.

The potential distribution for this variation in bias is displayed in figure 13. Again, as in figure 12, figures 13a and 13b contain the same data, the difference between the two is the curve that is emphasized. In figure 13a, the data **just prior to the current drop** is emphasized, whereas in figure 13b, the data **immediately following the current drop** is emphasized. In going from the emitter to the collector we see the buildup of a notch potential. The notch potential arises from the buildup of charge on the emitter side of the double barrier structure.

There are some very important features about the bias dependence of the potential energy profiles. First, the bias was changed in equal increments of potential energy, in this case by an amount k_BT. Initially, the **change** in potential energy **between the potential barriers** is small. However, the bottom of the conduction band between the barriers decreases rapidly with changes in bias. As carriers begin to accumulate on the emitter side of the barrier, and between the double barriers the potential difference **between the potential barriers** increases, but the **change in energy of the bottom of the band** changes insignificantly with respect to bias. This small change is a consequence of the large buildup of charge within the quantum well. However, when the carriers leave the quantum well and the current executes a precipitous drop the change in energy of the bottom of the band is almost as great as the change in applied potential energy.

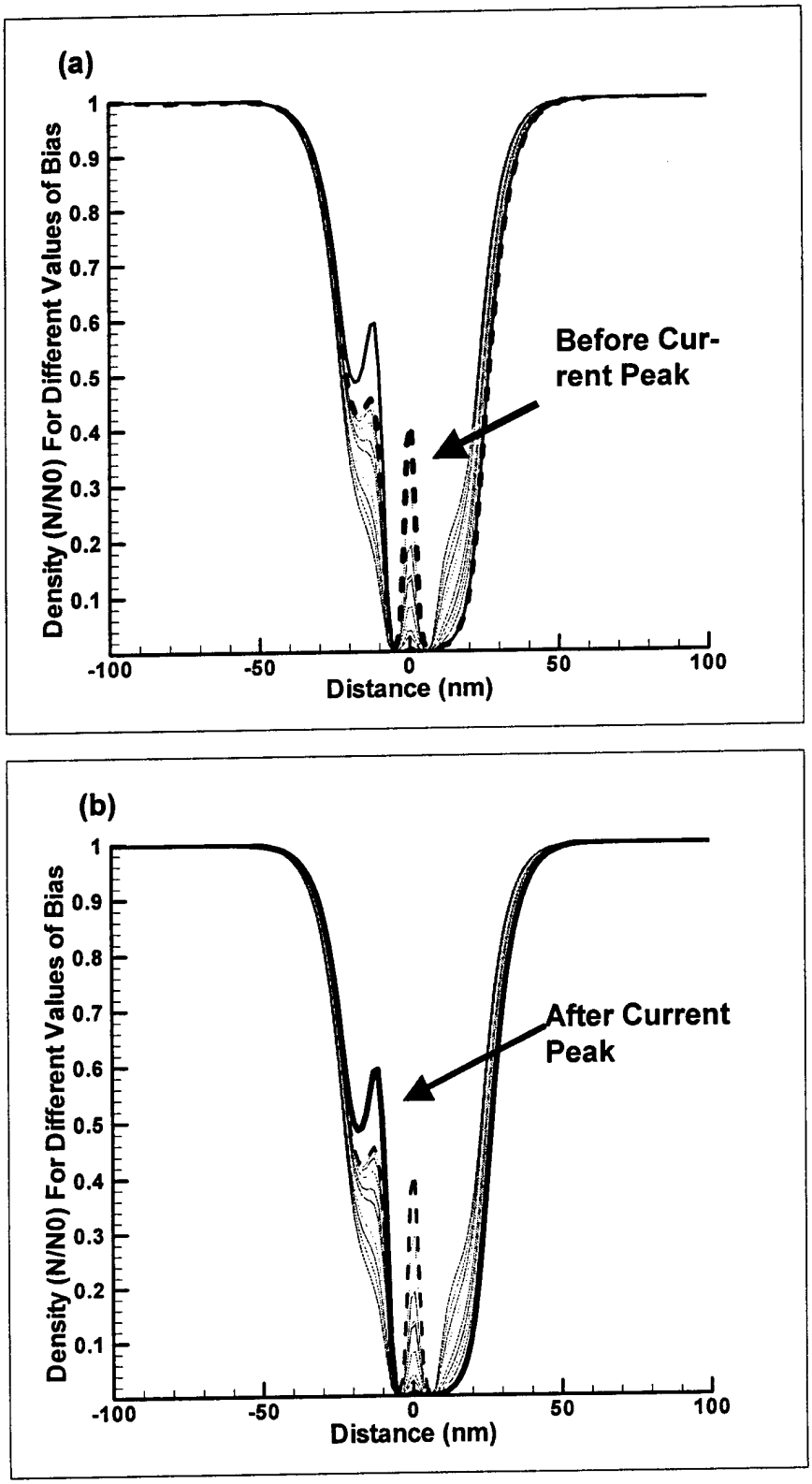

Figure 12. Density distribution as a function of bias. Figure 12a highlights the density prior to the drop in current. Figure 12b, highlights the density immediately following the drop in current.

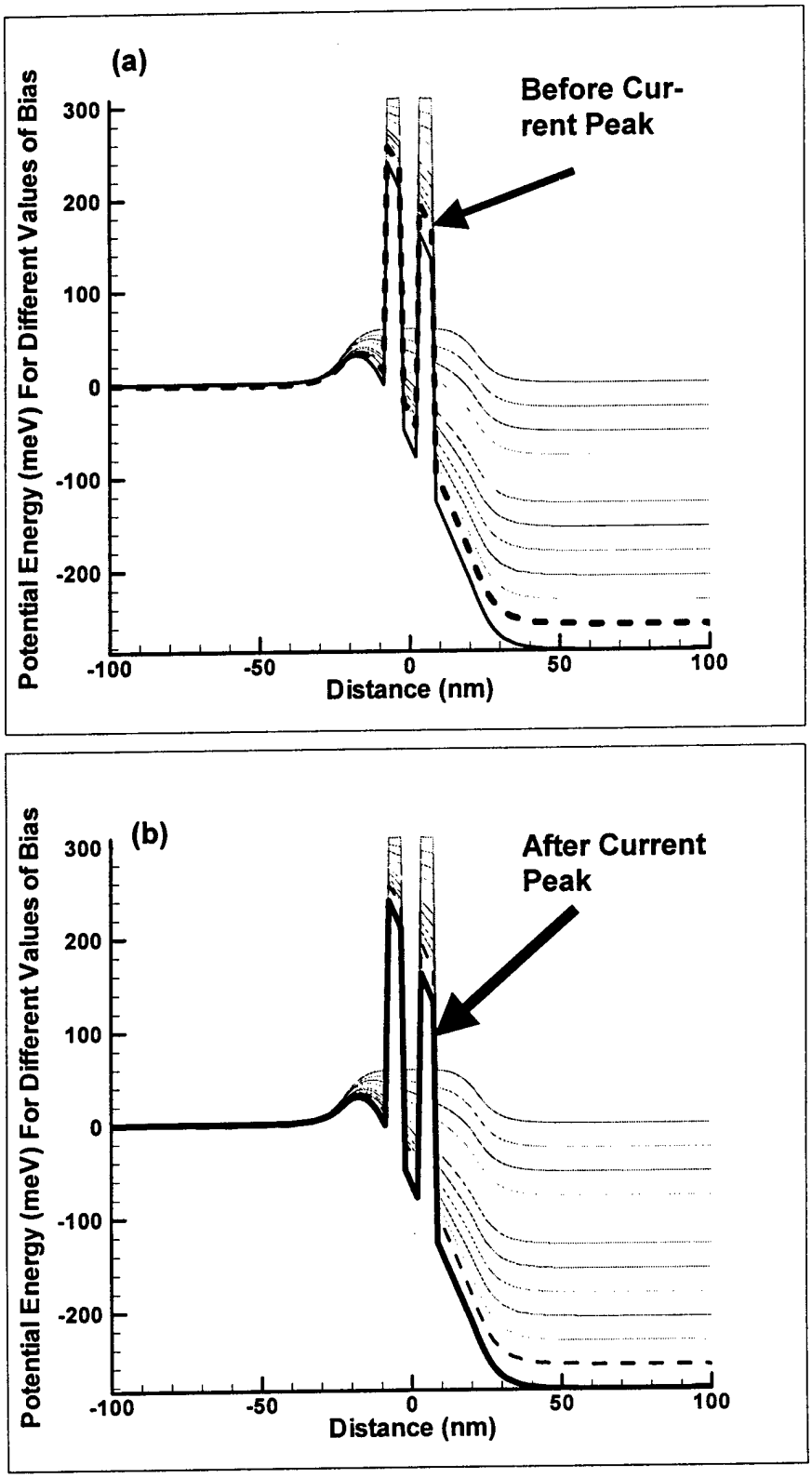

Figure 13. Potential energy distribution as a function of bias. Figure 13a highlights the potential prior to the drop in current. Figure 13b, highlights the potential immediately following the drop in current.

4.9 Transient Simulations-Display of Damped Current Oscillations

The heart of the study is the ability to perform transient calculations. This we have succeeded in doing. Indeed in demonstrating this capability we performed switching calculations in which we changed the potential drop across the device at a specified rate and watched the evolution of the space charge and hence the transient current profile.

The transient calculations were performed for the standard 200nm structure in which the peak dc current occurred at a voltage of $-10k_BT$. For this calculation we switched the voltage from zero to $-20k_BT$ and back to zero at a controlled rate. In other words we examined the response of the device to an approximate square wave (the nature of the leading and trailing edge of the pulse is determined by the rate of change of applied bias). The situation well into the pulse after the voltage changed from $-20k_BT$ to zero is displayed in figures 14 and 15. For this calculation the applied bias was changed in one time step ($25fs$).

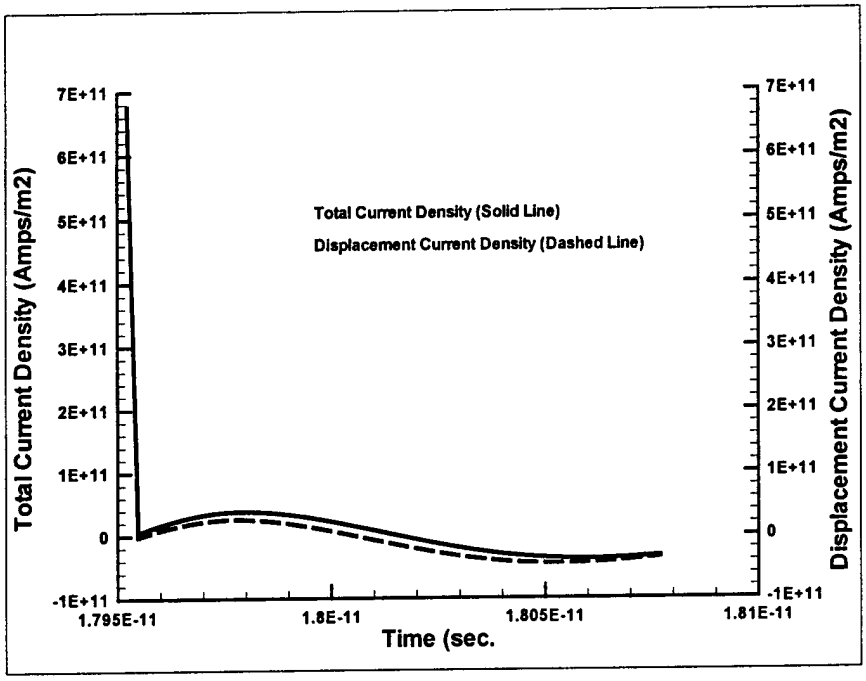

Figure 14. Transient current following a change in bias from $-20k_BT$ to zero.

The transient current following this change in applied bias is made up of two contributions:

1. a particle current $\mathbf{j}(\mathbf{r},t) = -(e/4\pi^3)\int d^3k\,(\hbar\mathbf{k}/m)\,f_W(\mathbf{k},\mathbf{r},t)$ and
2. a displacement current $(\varepsilon/e)\partial^2 V_{Poisson}/\partial t\partial x$

In the above $V_{Poisson}$ is the potential energy arising from Poisson's equation. The displacement current contribution is somewhat exaggerated in this calculation; and is a consequence of the imposed displaced Fermi distribution boundary conditions. The displacement contribution tends to dominate the initial current transient. As mentioned earlier, this boundary condition has been replaced by the $\partial f/\partial x = 0$ condition, which should yield realistic displacement current contributions.

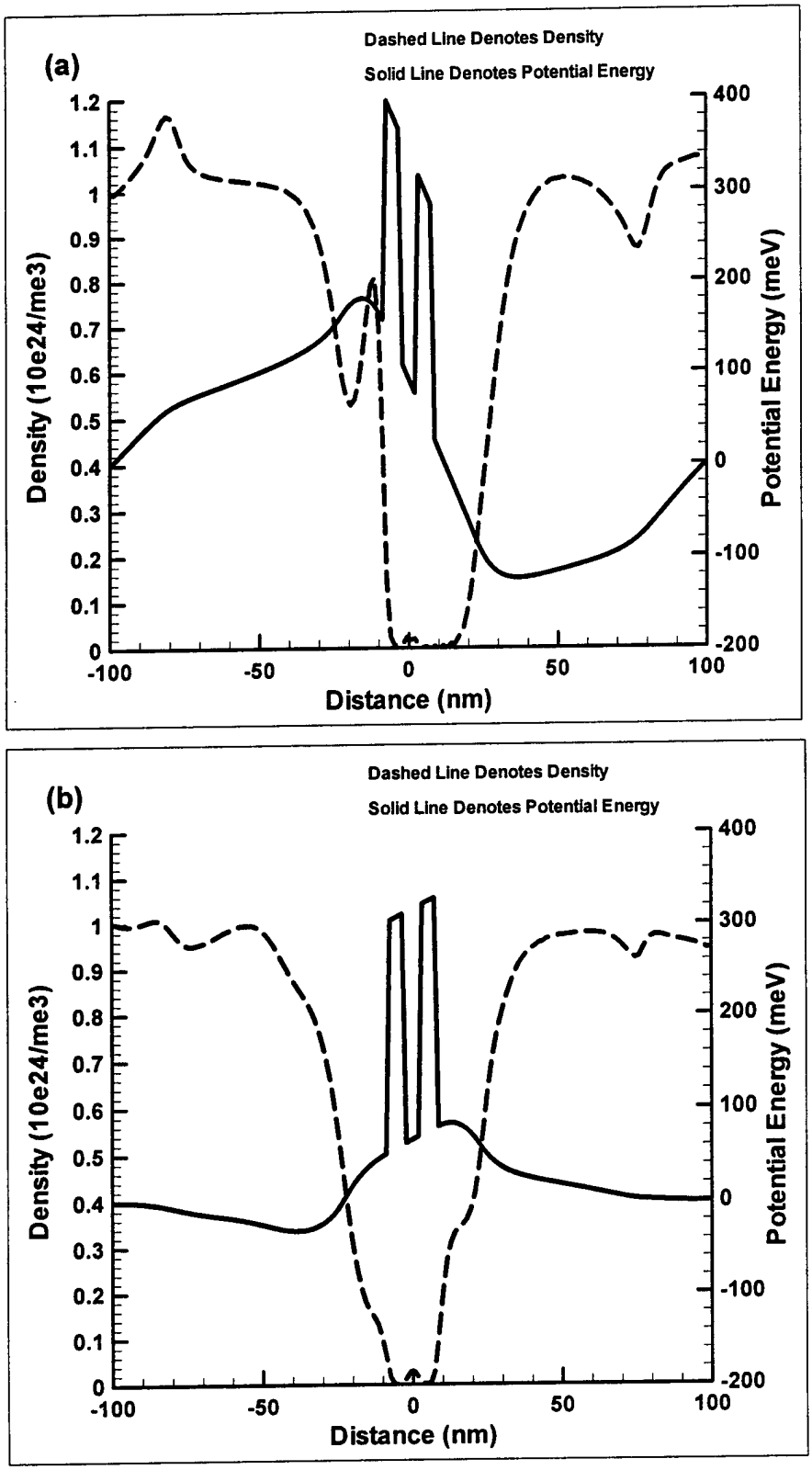

Figure 15. Transient density and potential energy distribution associated with the current time profile of figure transient. For figure 15a t=17.9752ps. For figure 15b, t=18.0770 ps

The total and displacement current contributions are displayed in figure 14 (the scales are the same for both axes), where we observe that there is a damped current oscillation, with negative and positive values centered about zero. Recall, in steady state the transient contribution is zero. The negative and positive values of current are associated with the displacement currents, which in turn are determined by the value and sign of the electric field at the emitter and collector contacts. This is illustrated in figures 15a and 15b, which represent snapshots of the potential energy and space charge distributions, immediately after the voltage change and at a later time (indicated in the figure) before the transients have disappeared.

To gain some insight into this result let us recall that at very high values of bias **there is significant charge accumulation on the emitter side** of the double barrier, with very little charge between within the quantum well. At low values of bias there isn't any significant accumulation for this structure. This means that the switch must allow for the removal of this excess charge from the device. If we examine figure 15a shortly after the bias has been abruptly changed to zero, we see significant charge accumulation on the emitter side of the double barrier and a very large and positive change in the potential. At the later time, figure 15b most of the excess accumulated charge has left the device and the change in potential energy at boundary is much smaller. Indeed the sign of the electric field at the boundaries has been altered. **This change in sign of the field at the cathode and anode boundaries is a major contributor to the change in the sign of the current.** ***Thus we see that there is a significant transient capability.*** **These calculations will provide us with a calculation of the hysterisis in the current.**

4.10 Comments on Accuracy of Calculation

We point out that the calculations performed above were for a square mesh with 150x150 grid points. We have run calculations with a maximum of 200x200, which resulted in improved accuracy. The amount of memory needed for larger grid sizes is shown in the below table. It appears that we shouldn't have any difficulty with today's' machines to get a grid of 500x500.

GRID	RAM (MG)
200 x 200	195
250 x 250	379
300 x 300	654
350 x 350	1037
400 x 400	1546
450 x 450	2200
500 x 500	3016

4.11 The User Interface

The user interface is currently under development. Presently the software is executed on at least four of SRA's Windows NT workstations using a UNIX shell with data entered through a *'namelist'* interface. This is basically a text-based entry. This type of interface is one that is routinely used at SRA for its Computational Fluid Dynamics Codes. An abbreviated form of this *'namelist'* interface is included below. The purpose of this inclusion is to identify the capabilities of the algorithm. The input is described next.

All data is entered into this text file. If the calculation starts from scratch it is necessary to identify plot files, data files and restart files. The restart files permit a continuation of previous runs.

1. Line 1 identifies a restart file that was saved from a previous run. If the calculation starts from scratch, this file does not exit.
2. Line 2 is a data file that is rewritten at the end of a calculation and functions as a restart for a subsequent calculation.
3. Line 3 identifies a data file for displaying the Wigner distribution.
4. Line 4 is a data file that contains all of the one-dimensional density, potential energy plots, etc.
5. Line 5 is a data file for the transient current versus time data.
6. Line 6 is a file that contains a summary of the calculation being performed including both input and output information. The file also contains diagnostics.
7. Line 7 includes a flag for setting the calculation as one that either starts from scratch, or is a continuation of a previous calculation.
8. This entry determines the number of time steps in the calculation.
9. This entry determines the actual time step. Since the algorithm is a transient algorithm, accurate transients are obtained by taking very small time steps.
10. This entry determines the rate at which the bias is changed. A very large value, indeed the one shown here results in a bias change in one time step. This number can be varied to determine the effect of rise time on the transient response of the device to an excitation.
11. This entry represents the number of momentum grid points.
12. This entry represents the number of spatial grid points.
13. The device length in meters.
14. The ambient temperature in degrees K.
15. We assume a phenomenological relaxation time in this study. The value entered here is the nominal value in the region where the barriers are present.
16. This phenomenological relaxation time is taken to represent the reservoir relaxation time. We have chosen a wide variety of values for this scattering time in an effort to gauge its significance.
17. This number, as a percentage of $1/2\times DEVICEL$ is identified as the region, on the emitter side where the scattering time is represented by $T01$.
18. The transition from $T01$ to $T0$ takes place over the distance $PER1\times 1/2\times DEVICEL < x < PER2\times 1/2\times DEVICEL$.
19. This entry is similar to that of line 17, but for the collector side of the device.
20. This entry is similar to that of line 18, but for the collector side of the device.
21. This number as a percentage of $1/2\times DEVICEL$ represents that percentage of the emitter side that is treated classically, i.e., the Wigner equation contains only classical contributions.
22. Rate of transition from the classical to the quantum mechanical region.
23. The number of square barriers in the calculation. The location of the center of the first barrier relative to the center of the device in meters.
24. The barrier height in electron volts.
25. The width of the barrier in meters
26. The location of the second barrier relative to the center of the device.

27. The height of the second barrier in electron volts.
28. The width of the second barrier in meters.
29. Critical time steps for obtaining the equilibrium Wigner distribution. For $IDT1$ time steps the calculation proceeds without any barriers. From time step $IDT1$ to $IDT2$ the barrier is increased to the value specified in lines 25 and 28. $NEXTRA$ are the number of additional time steps taken for convergence of the equilibrium solution. The total numbers of time steps to equilibrium are $IDT2 + NEXTRA$. (Equilibrium does not require any dissipation. Nevertheless, to achieve equilibrium we have found it necessary to incorporate dissipation for a finite number of time steps and then remove the dissipation from the calculation. For our present calculations, dissipation is included for the first 50 time steps and then discarded.)
30. Flag for setting the emitter boundary condition on the Wigner function. When $IEQBC(1,1,1) = 1$, a displaced Fermi distribution is used on the emitter boundary. When $IEQBC(1,1,1) = 101$, the normal derivative of the Wigner function is set to zero.
31. Similar to Line 31, but for the collector boundary.
32. Potential function boundary condition on the emitter side of the devices. When the flag is set to 3, the value of the potential energy on the emitter side is set.
33. Similar to line 33, but for the collector side of the device.
34. Value of the potential energy on the emitter side of the device of the device in multiples of $k_B T$.
35. Similar to line 35, but for the collector side of the device.
36. Flag is for the doping profile. When $IRHOCASE = 0$ there is no doping. When the flag is set to 1, the doping is constant. When the doping is set to 2, the doping is a function of position.
37. Beginning of the doping variation on the emitter side of the device, relative to the center of the device. Distance is in meters.
38. End of the doping variation on the emitter side of the device, relative to the center of the device. Distance is in meters.
39. Similar to line 39 but for the collector side of the device.
40. Similar to line 38 but for the emitter side of the device.
41. Density at the symmetric center of the device, in $1/m^3$.
42. Flag representing the way the Poisson potential energy is included in the Wigner equation. If $INTPOT = 0$, the contribution is treated as in the Boltzmann equation. If the flag is set to 1, the contribution is treated via the Wigner integral.
43. Flag determining how dissipation is treated. If $INORM = 0$, we deal with the standard relaxation time approximation. If the flag is set to 1 we deal with a relaxation time approximation in which the local particle density is conserved. If the flag is set to 2, we have a combination of the previous two conditions.

Also under development is an interface for access as a Microsoft Windows application. We have already developed another product that is fully executable in the Microsoft platform with GUI entries. This product, called QHD-CAD also includes a plot package. The windows interface that is currently under development under the Phase I study should be completed during the first part of the Phase II study, with an interface

structure very similar to the QHD-CAD interface. The QHD-CAD is available from the SRA website: http://www.srassoc.com.

```
 &READ1

 1 RESTFILE = 'E:\Wigner Simulations\restart\old_name.r',     Read a restart file enabling a continuation from a previous run
 2 RUNFILE  = 'E:\Wigner Simulations\restart\new_name.r',     Write a restart file enabling a continuation for a future run
 3 PLOTFILE = 'E:\Wigner Simulations\plot\plot_name.dat',     Write a file for plotting the Wigner distribution function
 4 WIGFILE  = 'E:\Wigner Simulations\plot\wig_name.dat',      Write a file for plotting the density, potential energy, electric field, current, etc.
 5 CURFILE  = 'E:\Wigner Simulations\plot\cur_name.dat',      Write a file for plotting current versus time
 6 OUTFILE  = 'E:\Wigner Simulations\rundir\new_name.pr',     Write a summary file

 7 IREST =0,                                                 Flag for running an equilibrium or nonequilibrium calculation.
                                                             For equilibrium flag is '0'.  For nonequilibrium flag is '1'.

 8 NT = 100,                                                 Number of interations

 9 DT = 40, DTMIN = 40, DTMAX =1000                          Time Step Control: Initial value, minimum value, maximum value
10 TRAT = 1.0e+20,                                           Rate at which applied bias is changed

11 MPOS = 150,                                               Number of momentum grid points
12 NMOM = 150,                                               Number of position grid points
13 DEVICEL = 200.0E-09,                                      Device length in nanomenters
14 TEMP = 300.0,                                             Ambient temperature in degrees K

15 T0 = 1.0E-13,                                             Nominal scattering time using the relaxation time approximation (in sec.)
16 T01 = 1.0E-13,                                            Reservoir region scattering time (in sec.)
17 PER1 = 15.0,                                              Percent of emitter reservoir emitter region
18 PER2 = 25.0,                                              Transition to nominal scattering time
19 PER3 = 25.0,                                              Transition to nominal scattering time
20 PER4 = 15.0,                                              Percent of collector reservoir emitter region

21 NCLASS = 20,                                              Percentage of  left and right side of device treated
                                                             classically (no Wigner integral contribution)
22 ANORMF = 1.0,                                             Rate of transition from classical to quantum region with Wigner integral

23 NBARR = 2,                                                Number of barriers in the calculation
24 SIIN(1) = -5.0E-09                                        Location of the center of the first barrier (meters)
25 VBARRIER2(1) = 0.25                                       First barrier height (eV)
26 WBARRIER(1) = 5.0E-9                                      First barrier width (meters)

27 SIIN(2) = +5.0E-09                                        Location of the center of the second barrier (meters)
28 VBARRIER2(2) = 0.25                                       Second barrier height (eV)
29 WBARRIER(2) = 5.0E-9                                      Second barrier width (meters)

30 IDT1 = 25, IDT2 = 50, NEXTRA = 50,                        To reach equilibrium, first IDT1 time steps are without a barrier. Next IDT2
                                                             time steps are with a barrier. Final NEXTRA time steps are to obtain equilibrium

31 IEQBC(1,1,1) = 1,                                         Wigner function emitter boundary condition. When flag is 1, Fermi
                                                             distribution, when flag is 101, derivative boundary condition

32 IEQBC(2,1,1) = 1,                                         Wigner function collector boundary condition. When flag is 1, Fermi
                                                             distribution, when flag is 101, derivative boundary condition.

33 IEQBC(1,1,2) = 3,                                         Potential function boundary condition on emitter side of device (x=-L)
34 IEQBC(2,1,2) = 3,                                         Potential function boundary condition on collector side of device (x=+L)

35 PHI(1,2) =  0.0,                                          Value of potential energy on emitter boundary (in multiples of kT)
36 PHI(2,2) = -1.0,                                          Value of potential energy on collector boundary (in multiples of kT)

                                                             Flag for doping profile.  IRHOCASE=0, no doping, '1' doping is constant
37 IRHOCASE = 2,                                             2' doping is a function of position
38 DIST1 = -25.0E-09,                                        End of doping variation on the emitter side.  Distance (m) is measured from device center.
39 DIST2 = -20.0E-09,                                        Start of doping variation on the emitter side.  Distance (m) is measured from device center.
40 DIST3 =  20.0E-09,                                        Start of doping variation on the collector side.  Distance (m) is measured from device center.
41 DIST4 =  25.0E-09,                                        End of doping variation on the collector side.  Distance (m) is measured from device center.
42 RHO2P = 1.000005195635047E+21                             Doping in center of structure m^(-3)

43 INTPOT = 0,                                               Flag for representing the Poisson potential energy in Wigner's equation of motion:
                                                             INTPOT=0, it is represented as in the Boltzmann equation; INTPOT=1, integral representation

44 INORM = 1,                                                Flag for the dissipation term. INORM=0, standard relaxation time approximation,
                                                             INORM=1, weighted relaxation time approximation.  INORM=2, combination of '0' and '1'.

 &END
```

5. Recommendations

5.1 Material Systems and Relaxation Oscillators

In the Phase I proposal we asked: "Where do the above considerations take us?" We also pointed out that at a recent '**6.1 A° III-V Semiconductor Workshop,** held at NRL; M. Yoder [3] delivered a presentation that included InAs/AlSb/GaSb RTD circuits for high speed, and low power (see figure 16). A statement in the slide accompanying the circuit was that "RI (interband) TD/HFET integration yields compact, nanoelectronic logic elements with unprecedented performance".

One of the goals of the SBIR program is to simulate the time dependent operation of device/circuit combinations that will yield square or near square wave pulses at frequencies in the 100+ GHz range. The RTD relaxation oscillator is a strong candidate for this to take place. The types of material systems that should be considered for this relaxation oscillator are those displayed in figure 16.

The GaAs/AlGaAs and InGaAs/AlAs systems are the strong candidates when the focus is on **low power** at high frequencies, as there are more conventional devices if power is not a primary objective. A variation of the InGaAs/AlAs system has been studied in which, for example, a small number of InAs layers is placed in the symmetric center of the RTD. This has the effect of lowering the resonance energy and the peak current. The lower voltage is essential if low power is to be achieved.

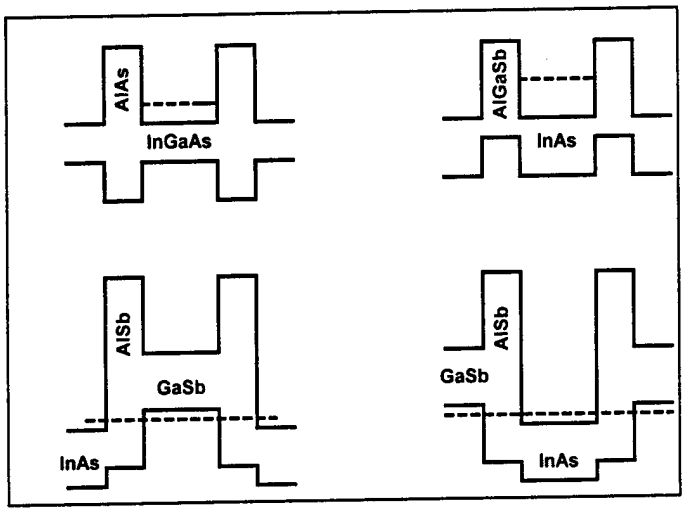

Figure 16. Various material combinations.

Structures such as those of figure 16 need to be incorporated into the Wigner algorithm for subsequent implementation in the simulation of a RTRO. Structures such as InGaAs /AlAs, GaAs/AlGaAs, or AlGaSb/InAs structures can readily be handled with the framework of the Wigner distribution without any major modifications in the scattering integrals. In this case electron and hole transport are coupled primarily through Poisson's equation. The situation with the InAs/AlSb/GaSb structure is more complex and requires that electron and hole transport be more intimately coupled, as is the case of an

Esaki diode. It is recommended that this work be undertaken to assure that simulation is a closely linked tool to device development.

5.2 Choosing a Demonstration of the Wigner Simulation Software.

All software designed to enhance the development of major technological goals must achieve a high level of credibility, before a significant number of users can be identified. To achieve this level of credibility it is necessary to choose a device that would be difficult to realistically design using any other software. It is recommended that the Wigner software be implemented to design a resonant tunneling relaxation oscillator, and that that the subsequent design be fabricated and tested in the laboratory. It is also recommended that the RTRO be considered as a component of a 100+GHz clock.

The design of the RTRO is a major effort and should proceed as follows:

1. With the RTD represented as a negative differential conductance device, rather than as a solution to the Wigner equation of motion, simulate the device in a transmission line representation of the circuit. The transmission line is the only approach that is suitable for high frequency simulations.
2. After a series of circuit and nominal device parameters have been established using the simpler model of the above paragraph, the negative differential conductivity representation of the RTD is replaced by the transient Wigner equation. That is, the Wigner equation of motion is solved simultaneously with the transmission line equations.
3. Because the Wigner simulations described in paragraph 2 are performed in conjunction with the *'SPICE'*-type studies many more calculations can be performed in the preliminary design of a device.
4. The SPICE type and Wigner simulations should then be configured for the design of a 100+GHZ clock.
5. Preliminary design information should then be transmitted to an organization that will perform the fabrication and oversee the testing of the device. In this regard, SRA has been in contact with Hughes Research Laboratories can fabricate and test the resonant oscillator in this configuration. There is also a distinct possibility that they will fabricate and test the device as an element in an integrated circuit. Hughes Research Laboratories have the materials capability with Dave Chow and also design and fabrication experience with Tom Broekaert. Tom Broekaert made RTD relaxation oscillators when he was at Raytheon (formerly Texas Instruments). These were monolithically integrated RTD clocks which are potentially much faster than the discrete prototypes demonstrated in [1].

5.3 Clock Issues, Particularly Speed Issues

There are problems with respect to high-speed clocks that must be addressed as we approach very high speeds. One problem is associated with the superior switching speeds of these high-speed devices. Fast edge rates of the new logic families are responsible for some of the problems encountered in their applications. These edge-rates rather than the clock rates set the required response of signal and power distribution systems. For example, below we list the upper-band-pass frequency at the 3-dB point for a low-

pass filter. The significance of this is that the third harmonic makes up approximately 10% of the amplitude of a linear ramp. Thus a system that does not have the bandwidth to pass the third harmonic content of an edge will attenuate the signal to some degree[13]. As can be seen as the rise time decreases the corresponding bandwidth increases.

Rise Time (ns)	Bandwidth (MHz)
1.00	350.00
2.00	175.00
3.00	116.00
4.00	87.50
5.00	70.00
6.00	58.40
7.00	50.00

Thus in the device simulations we need to consider the impact of the circuit elements as they affect the rise times.

Given the above constraints, what are the benchmarks for the high-speed clock? In the early 60s the Bell System developed the T-1 digital-communication-system [14] which generated a 1.544-megabit/sec pulsed digital signal. The signal was generated by multiplexing 24 voice channels. Each channel was sampled at a rate of 8,000 samples/second. Then the samples were quantized using eight-bit micro-law companding. The quantized samples from the 24 channels formed what was known as a frame, and since sampling was done at an 8-kHz rate, each frame occupied 1/8000 sec or 125 microseconds. There were 192 information and signaling bits in each frame (24x8) and a 193rd bit was added for frame synchronization. This framing signal was a pattern of 1's and 0's in every 193rd position. The product of 193 bits per frame and 8000 frames per second yielded a transmission rate of 1.544Mbits/sec. (Frame synchronization can be accomplished by transmitting a very distinctive waveform at the start of each frame, much as a comma is used to separate phrases or a period is used to separate sentences.) Extrapolating these numbers we see that at 1Mbit/sec, with 4 bits per frame, we require a sampling rate of 250,000 frames per second.

The exciting feature is that with RTDs it is realistic to expect sampling rates in excess of 100 G/sec. Then with effective bits well in excess of the '4' expected now, we are looking at transmitting 0.4Tb/sec of data.

If we can develop a robust device physics with RTDs operating in excess of 100 GHz, then the 0.4 Tb/sec data transmission is a realistic goal.

5.4 Concluding Recommendation

The broad recommendation is to continue the development of a transient, validated Wigner simulation capability that is

- portable,
- platform independent,
- affordable, and easy to use to provide the major design information for resonant tunneling devices, with an immediate goal of providing design features for the 0.4 Tb/sec data transmission

6 References

1. Verghese, S., C.D. Parker, and E.R. Brown, *Phase noise of a resonant-tunnelng relaxation oscillator.* Applied Physics Letters, 1998. **72**(20): p. 2550-2552.
2. Jin, B.B., X.R. Wu, and L. Kang, *A hybrid superconductor/GaAs MESFET microwave oscillator at 10.6 GHz.* Cryogenics, 1996. **36**(December): p. 993-995.
3. Yoder, M.N., *Future Electronics Requirements of DoD: RF Digital Microwave/Millimeter Wave Technology*, . 1998.
4. Mathews, R.H., *et al.*, *A new RTD-FET logic family.* Proceedings of the IEEE, 1999. **87**(4): p. 596-605.
5. Esaki, L., *New Phenomenon in Narrow Germanium p-n Junctions.* The Physcial Review, 1958. **109**(2): p. 603-604.
6. Weide, D.W., *et al.*, Applied Physics Letters, 1993. **62**: p. 22.
7. Shaw, M.P., H.L. Grubin, and P.R. Solomon, *The Gunn-Hilsum Effect.* 1979, New York: Academic Press. 250.
8. Scott, A., *Active and Nonlinear Wave Propagation In Electronics.* 1970, New York: Wiley-Interscience. 326.
9. Wigner, E., *On the Quantum Correction for Thermodynamic Equilibrium.* Physical Review, 1932. **40**: p. 749-759.
10. Blount, E.I., Physical Review, 1959. **114**: p. 418.
11. Tosima, S., J.J. Quinn, and M.A. Lampert, Physical Review, 1965. **137**: p. A883.
12. Tsuchiya, H. and M. Ogawa, IEEE Transactions on Electron Devices, 1991. **38**: p. 1246.
13. Buchanan, J.E., *CMOS/TTL Digital Systems Design.* 1990, New York: McGrraw-Hill Publishing Company. 258.
14. Roden, M.S., *Analog and Digital Communication Systems.* Fourth ed. 1996, Upper Saddle River, New Jersey: Prentice Hall. 560.